Renewable Energy 255 (2025) 123698

Contents lists available at ScienceDirect

Renewable Energy

journal homepage: www.elsevier.com/locate/renene

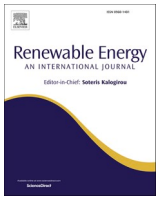

A novel efficient solar-gas assisted hydrogen-electricity cogeneration system based on photo-thermal energy cascade conversion: modeling and performance analysis

Zihui Xu, Shiquan Shan *, Biao Zhang, Zhihua Wang, Zhijun Zhou, Kefa Cen

State Key Laboratory of Clean Energy Utilization, Zhejiang University, Hangzhou, 310027, China

ARTICLE INFO

Keywords:
Solar-gas assisted
Photo-thermal energy
Cascade conversion
Hydrogen-electricity cogeneration
Thermo-photovoltaics
Copper-chlorine cycle

ABSTRACT

In this study, an efficient solar-gas assisted hydrogen-electricity cogeneration system is proposed. It constructs from thermos-photovoltaics (TPV), supercritical carbon dioxide Brayton cycle (SCO_2-BC) and Cu-Cl chemical cycle according to photo-thermal energy cascade conversion. A system thermophysical analysis model is established and the effect of parameters on the electricity/hydrogen production efficiency and irreversible loss are investigated based on second law. The design concept is proposed that using by-product oxygen from hydrogen generation to assist combustion for system stable running. Besides, the superiority of the novel system is discussed by comparing with different configurations. The results show that the concentration ratio, TPV area, and turbine inlet temperature can be used to adjust the ratio of electricity/hydrogen production. In actual applications, the system can keep continuous and efficient by appropriately increasing the oxygen ratio when solar energy input is insufficient. The second law analysis shows the exergy destruction factor of TPV module is the largest (about 30 %), followed by receiver module (11.68 %). The system energy efficiency can reach 61.26 % for electricity/hydrogen cogeneration, and the equivalent electrical efficiency can reach 52.98 %, which has obvious advantages compared with other different system configurations. This work provides guidance for the development of solar high-efficiency hydrogen/electricity cogeneration technology.

1. Introduction

Widespread consumption of fossil fuels has resulted in substantial greenhouse gas emissions, causing global warming and environmental damage. Energy and environmental issues are gradually coming into focus. As of 2021, a total of 124 countries have pledged to achieve carbon neutrality by 2050 or 2060 [1], committing to optimizing the existing energy structure and developing renewable energy system. Therefore, solar energy has been regarded as one of the most promising green energy since its cleanliness, wide distribution, easily accessible and huge reserves. At present, solar power technologies mainly include solar photovoltaic (PV) and solar thermal power generation [2]. However, PV cells can only utilize high-grade solar energy within a specific waveband, large amounts of solar energy are wasted. High-temperature solar energy concentration and harvest are costly and difficult to achieve efficient conversion. Besides, overcoming periodic fluctuations must be considered in solar energy utilization. In a word, realizing efficient and stable conversion of solar energy is the key to achieving large-scale application.

In the past period, it has been proposed the solar-fuel assisted system to improve conversion efficiency, overcome the fluctuations of the solar energy utilization and save fossil fuels. Milanese et al. [3] proposed a new type of solar-aided coal-fired power plant, which is composed of a trough collector field based on gas-phase nanofluids and coupled with a flameless coal burner. Numerical simulation results revealed the solar input could not only elevate the recirculation zone temperature, yielded uniform chemical products and temperature conditions, but also greatly reduced NO_x emissions. Chinnici et al. [4] designed a hybrid combustion device that directly couples a solar cavity receiver with combustor, and experimentally explored the economic benefits of three operation modes. It was found that using solar-fuel assisted modes could greatly save energy and cost in the same power generation conditions. In addition, most scholars designed solar-fuel assisted thermal power cycle (TPC) based on combustion. Zhao et al. [5] designed a solar-coal assisted Rankine cycle. Calculations and optimization of solar collector mirror field size and energy storage capacity in the solar-coal assisted power device have also been carried out. Rovira et al. [6] designed a gas-steam

* Corresponding author.
E-mail address: shiquan1204@zju.edu.cn (S. Shan).

https://doi.org/10.1016/j.renene.2025.123698
Received 6 December 2024; Received in revised form 28 April 2025; Accepted 7 June 2025
Available online 10 June 2025

Nomenclature

C	concentration ratio
C_p	specific heat (J/(kg·K))
$\dot{E}^D$	exergy destruction (kW)
$\dot{E}x$	exergy (kW)
FF	filling factor
H	surface heat transfer coefficient (W/(m^2·K))
h	enthalpy (kJ/kg)
I_s	solar radiation intensity (W/m^2)
J_{SC}	short-circuit current (A)
LHV	lower heating value (kJ/kg or kJ/mol)
$\dot{m}$	mass flow rate (kg/s)
P	power (kW)
P_1	solar input power (kW)
p	pressure (MPa)
r	split ratio
R_{O_2}	oxygen ratio
S_1	tube receiver area (m^2)
S_2	combustion chamber area (m^2)
T	temperature (K)
V_{OC}	open-circuit voltage (V)

Geek symbols

λ	wavelength (nm)
λ_c	cut-off wavelength of the filter (nm)
ε	Recuperator emissivity
ε_{ex}	heat-exchange coefficient of heat exchanger
η	efficiency (%)
φ	exergy destruction factor

Subscripts

af	adiabatic flame
cell	PV cell
ch	chemical
com	compressor
cp	combustion product
el	generate power
em	emitter
ex	exergy
flt	filter
g	flue gas
in	input
out	output
ph	physical
sec	secondary energy
sys	system
w	wall of combustion chamber
0	ambient
1–11	flow number

Abbreviations

BC	Brayton cycle
CC	combustion chamber
Cu-Cl	copper-chlorine
HTR	high-temperature recuperator
LTR	low-temperature recuperator
MC	main-compressor
PV	photovoltaic
RC	re-compressor
Ref Sys	reference system
SCO_2	supercritical carbon dioxide
T	turbine
TR	tube receiver
TPV	thermo-photovoltaic

combined cycle with solar and fuel complement, they found that preheating air before combustion chamber can not only reduce fuel consumption but also improve the steam turbine efficiency. Bustamante et al. [7] analyzed the performance of solar-biogas assisted power generation system, it indicated that the complementary system can better meet its own industrial energy requirements. Xue et al. [8] proposed a hydrogen-electricity cogeneration system based on thermochemical complementary of coal and solar energy. Compared with the conventional hydrogen-electricity cogeneration system which using non-complementary coal gasification and concentrating solar power generation, the efficiency of the thermochemical complementary system is greater than 4.91 %. Wang et al. [9] proposed a new combined cooling, heating and power (CCHP) system which integrates solar thermochemical process, and they found that the solar-methane assisted design can increase the system output. Recently, Wang et al. [10] proposed a system of supercritical carbon dioxide Brayton cycle (SCO_2-BC) driven by solar-aided biomass combustion. Numerical calculations results indicated that the proportion of solar energy supply is as high as 36.4 % in summer, and the solar-to-electric efficiency is within 21.9–23.7 % in representative days. It can be found the solar-fuel assisted design could not only optimize the combustion conditions in combustion chamber, reduce fossil fuel consumption and pollutant emissions, but also convert low-grade solar energy which is difficult to be efficiently utilized into high-grade thermal energy. It is undoubtedly a key technology to improve solar energy conversion efficiency.

For TPC, Shan et al. [11] noticed that it is unable to scientifically and rationally match high-temperature combustion condition since the limited power cycle parameters, resulting in a large exergy loss. Therefore, they proposed the concept of photo-thermal energy cascade conversion: (1) The high temperature energy generated by fuel combustion is firstly converted into thermal radiation, and converted by thermo-photovoltaic (TPV) device. (2) The remaining thermal energy enters the TPC for power generation. Shan et al. [12] proposed a cascade TPV system with oxy-fuel combustion. The system performance was improved by oxy-fuel combustion and cascade design, and the system efficiency reaches 26.6 %. In order to further utilize the thermal energy with medium or low temperature, a system coupling TPV and Brayton-Rankine cycle was also proposed [13]. Numerical simulation results indicate that the system output power also showed an increasing trend with the oxygen ratio. It was demonstrated that the combination of TPV (based on combustion) and TPC has obvious advantages in energy conversion and utilization. Meanwhile, the cascade conversion and utilization of photo-thermal energy can overcome the temperature mismatch between flue gas and the working fluid in TPC. It should be mentioned that the development of renewable energy assisted system is important to future application. However, few studies have focused on the solar-fuel assisted TPV system and the corresponding photo-thermal energy cascade conversion system.

For the application of secondary energy, the electric energy is difficult for storage, primarily due to the reliance on costly electrochemical cells. Hence, electricity production also needs to be supplied to the power grid in real time. In contrast, hydrogen energy, as an emerging secondary energy, has become a focus of attention since its high quality, reliable storage and transportation characteristics. Many energy systems have considered hydrogen-electricity cogeneration [14,15] to achieve efficient and stable energy production. For solar-fuel assisted thermal power system, it will generate both electrical and thermal energy with different quality. This is much more suitable for thermochemical cycle

hydrogen production. Compared with electrolysis hydrogen production, thermochemical cycle technologies, such as the copper-chlorine (Cu-Cl) cycle, utilize electricity and heat more effectively. Operating at relatively low temperatures around 530 °C [16], the Cu-Cl cycle is favored for its cost-effectiveness, environmental sustainability [17], and less stringent requirements on equipment materials and product separation processes [18]. The cycle typically involves three to five steps; notably, the four-step cycle, comprising hydrolysis, pyrolysis, electrolysis, and drying, offers superior energy efficiency over the other variants [19]. This route necessitates high-quality electric energy for electrolysis and accommodates multiple thermochemical reactions with diverse temperature demands. Moreover, the Cu-Cl cycle uses energy at varying grades simultaneously, aligning with the second law of thermodynamics through energy cascade utilization. In recent developments, researchers have explored various configurations to supply the requisite energies for Cu-Cl cycle. Notable studies include the use of concentrated solar radiation and alternative power supply systems. For instance, Ishaq et al. [20] investigated a solar-wind hybrid system for hydrogen production where a solar heliostat field and a wind turbine provide the necessary thermal and electric energy, respectively. On the other hand, Sayyaadi et al. [21] directly extracted electricity from the grid to maintain a continuous and reliable power supply. Furthermore, Sadeghi et al. [22] have proposed an innovative solar-driven Cu-Cl cycle system utilizing air as the heat transfer fluid in solar towers, alongside a solar-driven Rankine cycle for electricity generation needed for electrochemical reactions. Coulibaly et al. [23] powered the Cu-Cl cycle by a parabolic trough collector power plant and a molten carbonate fuel cell. Sadeghi et al. [24] investigated the integration between a standalone solar power tower (SPT) and four-step Cu-Cl cycle with LiNaK high-temperature carbonate molten salt, the solar-driven supercritical Rankine cycle is used for power supply. In recent years, SCO_2-BC has seen extensive application in solar-driven thermochemical hydrogen production, owing to its numerous advantages including high efficiency [25], enhanced flexibility [26], compactness [27], and compatibility with concentrated solar power (CSP) systems [28]. Sun et al. [29] designed a solar hydrogen production system that integrates a solar heliostat field, a receiver, a sulfur-iodine cycle, and a SCO_2-BC. Similarly, Zhang et al. [30] developed a system where a solar tower captures thermal energy to power a SCO_2-BC for electricity generation, which in turn drives Cu-Cl cycle. This system also employs the remaining thermal energy for staged heating in Cu-Cl cycle and incorporates an organic Rankine cycle (ORC) for recycling system waste heat. The SCO_2-BC is particularly effective with heat sources above 550 °C, offering thermal efficiency surpassing that of the supercritical steam cycle. However, it should be noted that existing research on integrating the solar-driven Cu-Cl cycle often ignored the energy quality difference between photo and thermal energy during energy conversion, leading to unreasonable utilization of high temperature energy. Additionally, there is no research on the photo-heat energy cascade utilization in solar-fuel assisted hydrogen production system.

Based on the literature review, solar-fuel assisted design is a key technology to convert low-grade solar energy into high-grade thermal energy and improve solar energy conversion efficiency. However, few scholars have conducted research on solar-fuel assisted TPV systems and the corresponding photo-thermal energy cascade conversion system. Moreover, researchers always ignored the quality difference between photo and thermal energy during energy conversion, and failed to utilize the high-temperature energy scientifically and effectively, resulting in the low energy efficiency. The total efficiency of the solar-driven sulfur-iodine cycle hydrogen production system proposed by Sun et al. [29] is 30.50 %. Sorgulu et al. [31] proposed a solar-driven hydrogen production integrated system based on the thermochemical cycle, the energy and exergy efficiencies are 26.1 % and 21.28 %, respectively. Song et al. [32] proposed a hydrogen production system driven by solar energy for a two-step thermochemical cycle and a solid oxide electrolysis cell (SOEC), with an exergy efficiency of 32 %. Against the above studies and problems, this study starts from the scientific theory of photo-thermal energy cascade utilization, and proposes an efficient hydrogen-electricity cogeneration system integrating a solar-gas assisted TPV, a SCO_2-BC, and a Cu-Cl cycle. The novelty of this study lies in: (1) Demonstrate how to combine solar energy with natural gas can enhance the energy grade and optimize the efficiency. (2) Convert energy of different qualities orderly and efficiently, and achieve complement and coupling of different energy types for different demands. (3) The system energy efficiency can reach 61.26 % for electricity/hydrogen cogeneration. As shown in Fig. 1, the proposed system initially converts

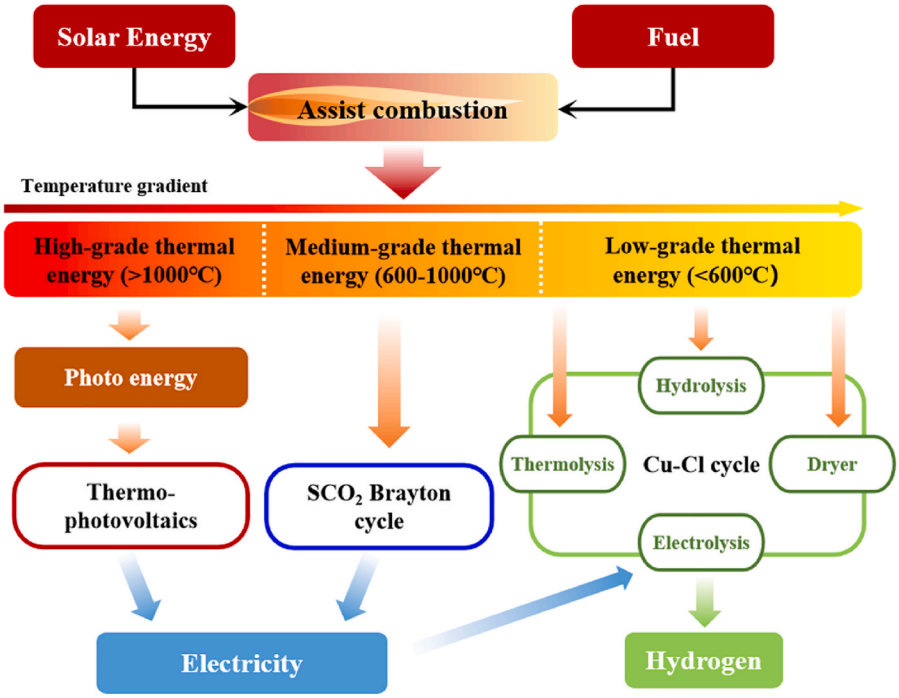

Fig. 1. Schematic diagram of the solar-fuel assisted hydrogen-electricity cogeneration system based on photo-thermal energy cascade conversion.

high-grade radiation energy from high-temperature combustion into electrical energy via photovoltaics. Subsequently, the remaining medium-grade thermal energy is harnessed through thermal power conversion, facilitating energy cascade conversion. According to the principles of energy quality matching, this approach facilitates the staged production of H_2 within the Cu-Cl cycle by supplying electric and thermal energies of varying qualities, thereby achieving complement and coupling of different energy types. The innovative work of this research is as follows: (1) A novel solar-gas assisted hydrogen-electricity cogeneration system based on photo-thermal energy cascade conversion is proposed, and a thermophysical model is established. (2) The influence of system parameters on the electricity/hydrogen production efficiency is analyzed, and the irreversible losses of the system are investigated. (3) The design concept is proposed that the by-product oxygen is used to assist combustion for stable operation, and the parameters analysis is conducted. (4) The rationality and superiority of the proposed system is discussed by comparing with alternative configurations. This study provides a specific case for the theoretical research on the energy cascade conversion of solar-gas complementary, and provides important guidance for the development and application of solar energy efficient hydrogen-electricity cogeneration technology.

2. System description

The system outlined in Fig. 2 comprises five primary modules: solar collector, combustion chamber (CC), TPV, SCO_2-BC and Cu-Cl cycle. In the solar collector module, the concentrator receives and focuses the sunlight on the tube receiver. The air is preheated by the sunlight in tube receiver before entering CC to assist combustion. In CC module, fuel and preheated air burn in CC, generating high-temperature flue gas. In the TPV module, the radiation energy P_{rad} generated by the combustion is emitted to the filter surface through the emitter, which is on the wall of CC. The radiation energy with a waveband matching the PV cell's band gap P_{flt} passes through the filter to reach the PV cell surface, and then outputs electrical energy. The radiation energy which does not match the band gap P_{back} cannot pass through the filter, and returns to CC to maintain the emitter surface temperature. In SCO_2-BC module, the inside CO_2 is heated by the high-temperature flue gas via heat exchanger to drive the turbine generating electricity. Meanwhile, the residual flue gas, after facilitating the SCO_2-BC, continues to provide thermal energy for various processes in the Cu-Cl module, including hydrolysis, pyrolysis, and drying processes. Electrical power generated from both the TPV and the SCO_2-BC is utilized for electrolysis within the Cu-Cl cycle, which produces hydrogen. The energy inputs of the system comprise solar energy and fuel, while its outputs comprise electricity and hydrogen. To streamline the development of the model, several certain reasonable assumptions are incorporated and shown as follows:

(1) The system is in a steady state;
(2) The ambient temperature is 300 K, and the pressure is 1 bar;
(3) Unless otherwise specified, the air is assumed to be 79 % N_2 and 21 % O_2;
(4) Air, fuel gas, O_2 and H_2 are ideal gases;
(5) The pressure drop is ignored in all heat exchangers and connection lines;
(6) Kinetic and potential energies are disregarded in analysis.

3. System models and methods

3.1. Model of solar collector

The solar collector in this study is composed of a concentrator and a tube receiver. The concentrator receives and focuses the sunlight on the tube receiver, and converts it into thermal energy in the working fluid (air). The solar radiation energy P_{sol} received is given by Ref. [33]:

$$P_{sol} = CI_sS_1 \tag{1}$$

where I_s is the solar radiation intensity, $I_s = 1000\ \mathrm{W/m^2}$.

In this study, air is preheated by the absorbed thermal radiation energy in the tube receiver. Here, thermal radiation effect is focused. The heat loss of the receiver surface is taken into account, while the others with less influence are ignored. Therefore, the energy balance model of the tube receiver can be written as [33]:

$$P_1 = CI_sS_1\alpha\rho - S_1\varepsilon_{TR}\sigma\left(T_{TR}^4 - T_0^4\right) \tag{2}$$

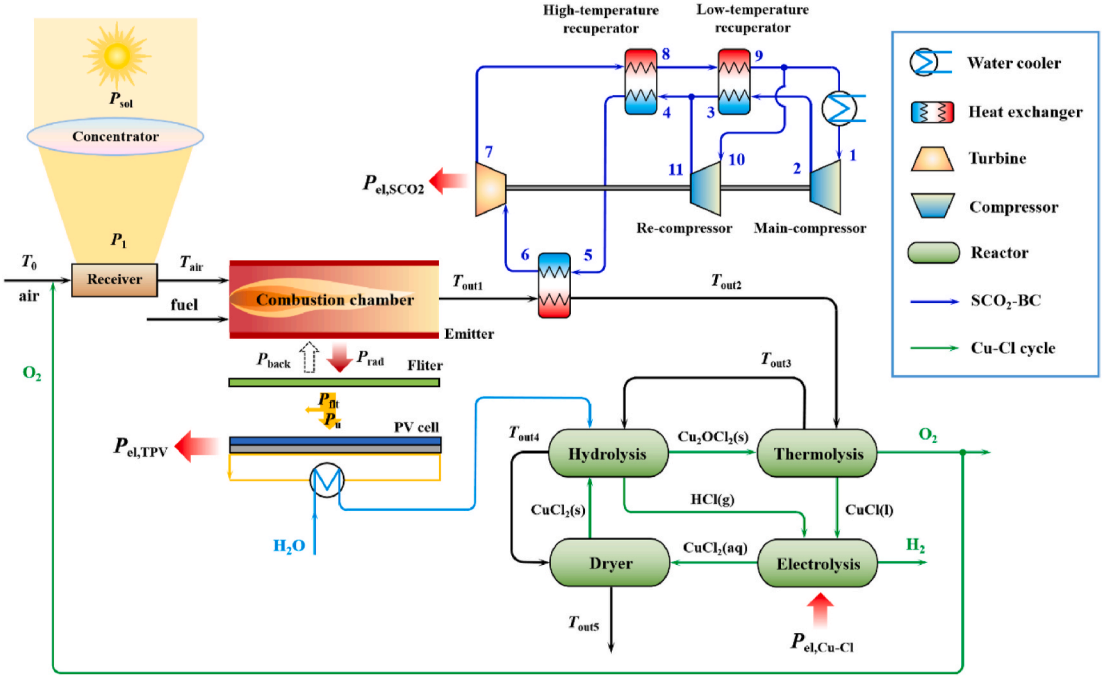

Fig. 2. Schematic diagram of the integrated system.

$$P_1 = \dot{m}_{air} \int_{T_0}^{T_{air}} C_p(\text{air}) dT \tag{3}$$

where ρ is the reflectivity of the concentrator surface, $\rho = 0.90$ [34]; α is the absorptivity of the tube receiver surface, $\alpha = 0.95$ [35]; ε_{TR} is the emissivity of the tube receiver surface, $\varepsilon_{TR} = 0.27$ [36].

The heat transfer coefficient η_{col} (assumed to be 1 in this study) between air and the surface of tube receiver can be written as [33]:

$$\eta_{col} = \frac{T_{air} - T_0}{T_{TR} - T_0} \tag{4}$$

3.2. Model of combustion chamber (CC)

In this research, the fuel input power was taken as 15 kW, the fuel is methane (CH_4, lower heating value $LHV = 50016$ kJ/kg), and the excess air coefficient was set as 1.1. The energy balance model calculation of the entire CC relies on our previous research [12,33]. CC is simplified as multiple juxtaposed cylinders with a radius of 0.04 m.

The total power input P_{in} is the sum of P_{sol} and the input power of the fuel P_{fuel} [12].

$$P_{in} = P_{fuel} + P_{sol} \tag{5}$$

The fuel (CH_4) input power P_{fuel} can be denoted as [12]:

$$P_{fuel} = \dot{m}_{fuel} \cdot LHV_{fuel} \tag{6}$$

The relationship between P_{fuel}, adiabatic flame temperature T_{af} and solar input power P_1 can be expressed by the following formula [12]:

$$\dot{m}_{cp} \int_{T_0}^{T_{af}} C_p(\text{cp}) dT = P_{fuel} + P_1 \tag{7}$$

where $\dot{m}_{cp}$ is the mass flow rate of the combustion products (flue gas); $C_p(\text{cp})$ is the specific heat of combustion products (flue gas), the calculation method of enthalpy of flue gas is based on Ref. [37]; T_0 is ambient temperature; T_{af} is obtained by a calculation program for the equilibrium products of hydrocarbon combustion [37].

The thermal balance between the high-temperature flue gas in CC and the emitter radiation can be expressed as follows [12]:

$$P_{flt} = \varepsilon_{sys}\sigma\left(T_g^4 - T_w^4\right)S_2 + H\left(T_g - T_w\right)S_2 \tag{8}$$

$$P_{flt} = \dot{m}_{cp} \int_{T_{out1}}^{T_{af}} C_p(\text{cp}) dT \tag{9}$$

$$T_w = T_{em} \tag{10}$$

where the wall temperature of CC T_w is approximately the same as the emitter wall temperature T_{em}; T_g is the average temperature of the flue gas in CC; T_{out1} is the TPV outlet flue gas temperature; H is the surface heat transfer coefficient between flue gas and the wall, $H = 180$ W/$(m^2 \cdot K)$ [12].

The radiative energy passing through the filter P_{flt} can be defined as [12]:

$$P_{flt} = \varepsilon_{em} S_2 \int_0^{\lambda_c} I_s(\lambda, T_{em}) d\lambda \tag{11}$$

where ε_{em} is the emissivity of the emitter, $\varepsilon_{em} = 0.9$ [38]; λ_c is the cut-off wavelength of the filter corresponding to the PV cell.

The system emissivity ε_{sys} is defined as [39]:

$$\varepsilon_{sys} = \frac{1}{\frac{1}{\varepsilon_w} + \frac{1}{\varepsilon_f} - 1} \tag{12}$$

where ε_w is the emissivity of furnace wall, $\varepsilon_w = 1$ [12]; ε_f is the flame emissivity, expressed as the weighted sum of the gas emissivity and particle emissivity [39]:

$$\varepsilon_f = m_{lu}\varepsilon_{lu} + (1 - m_{lu})\varepsilon_g \tag{13}$$

where m_{lu} is the ratio of the luminous particles, $m_{lu} = 0.1$; ε_{lu} is the emissivity of the luminous particles, $\varepsilon_{lu} = 0.85$ [39]; ε_g is mixed gas emissivity, which is calculated by the weighted-sum-of gray-gases (WSGG) model [40].

The relationship among T_g, T_{af} and T_{out1} can be written as [41]:

$$T_g^4 = rT_{out1}^4 \tag{14}$$

$$r = \frac{3}{\left(T_{out1}/T_{af}\right)^3 + \left(T_{out1}/T_{af}\right)^2 + T_{out1}/T_{af}} \tag{15}$$

3.3. Model of TPV cell

In this study, GaAs PV cell with band gap of 1.42 eV is investigated, and the cut-off wavelengths of the corresponding filter is 950 nm [42]. The output power $P_{el,TPV}$ of the PV cell can be defined as [12]:

$$P_{el,TPV} = V_{OC} \cdot FF \cdot J_{SC} \tag{16}$$

The short-circuit current J_{SC} can be computed as [12]:

$$J_{SC} = \int_0^{\lambda_c} \frac{q_0 \lambda}{hc} EQE(\lambda) I_S(\lambda) d\lambda \tag{17}$$

where EQE is the external quantum efficiency; q_0 is the elementary charge; h is the Planck constant; c is the speed of light.

The open circuit voltage V_{OC} can be written as [13]:

$$V_{OC} = \frac{\Gamma k T_0}{q_0} ln\left(\frac{J_{SC}}{J_0} + 1\right) \tag{18}$$

where k is the Boltzmann constant; Γ is the diode ideality factor, which is taken as 1 in this study [33]; T_0 is the surface temperature of the PV cell (constant 300 K); J_0 is the diode saturation current of the PV cell, which can be expressed as [43]:

$$J_0 = 1.5 \times 10^5 \, exp\left(\frac{-Eg}{kT_0}\right) \tag{19}$$

The filling factor FF can be calculated as [43]:

$$FF = \beta \frac{\nu - ln(\nu + 0.71)}{\nu + 1} \tag{20}$$

where β is the correction factor, which is taken as 0.96 [4]; ν is the normalized open-circuit voltage, which is given by Ref. [43]:

$$\nu = \frac{q_0}{kT_0} V_{OC} \tag{21}$$

The actual radiative energy reaching PV cell P_u is equal to the product of P_{flt} and the radiation view factor η_{VF}, which is generally related to the geometry of PV cell and the distance between emitter and PV cell. Because of the close distance between the emitter and the PV cell in this system, the η_{VF} can be regarded as 1 [12].

$$P_u = P_{flt}\eta_{VF} \tag{22}$$

PV cell efficiency can be defined as [43]:

$$\eta_{cell} = \frac{P_{el,TPV}}{P_u} \tag{23}$$

3.4. Model of SCO_2-BC

As presented in Fig. 2, the SCO_2-BC includes various steps: isentropic compression in the main-compressor (MC) (1–2), isobaric endothermic

in the low-temperature recuperator (LTR) (2–3), isobaric endothermic in the high-temperature recuperator (HTR) (4–5), isobaric endothermic in the heat exchanger (5–6), isentropic expansion (6–7), isobaric exothermic in HTR (7–8), isobaric exothermic in LTR (8–9), isentropic compression in the re-compressor (RC) (10–11) and isobaric exothermic (9–1).

Firstly, CO_2 is compressed in MC (1–2). The work done by MC on the system can be expressed as [44]:

$$P_{MC} = \frac{(1-r)\cdot\dot{m}_{SCO_2}\cdot(h_{2s}-h_1)}{\eta_{com,SCO_2}} \tag{24}$$

$$\eta_{com,SCO_2} = \frac{h_{2s}-h_1}{h_2-h_1} \tag{25}$$

where h_{2s} represents the isentropic enthalpy after pressurization in MC; η_{com,SCO_2} is the compressor efficiency, $\eta_{com,SCO_2} = 0.89$ [45,46]; $\dot{m}_{SCO_2}$ is CO_2 mass flow rate in the SCO_2-BC. In particular, the CO_2 mass flow rate in MC is $(1-r)\cdot\dot{m}_{SCO_2}$, and r is split ratio.

The compressed CO_2 recovers heat from flow 8 through LTR (2–3). The recovered heat can be expressed as [44]:

$$Q_{LTR} = (1-r)\cdot\dot{m}_{SCO_2}\cdot(h_3-h_2) = \dot{m}_{SCO_2}\cdot(h_8-h_9) \tag{26}$$

$$\varepsilon = \frac{h_8-h_9}{h_8-h_9(T_2,p_9)} \tag{27}$$

where $h_9(T_2,p_9)$ represents calculated based on the assumption that the heat flow 9 reaches the temperature T_2 after leaving the LTR [44]; ε is the recuperator ratio of recuperator, $\varepsilon = 0.95$ [45].

The flow 10 of the high-temperature flow 9 is compressed in RC (10–11), and the work done by RC on the system can be expressed as [44]:

$$P_{RC} = \frac{r\cdot\dot{m}_{SCO_2}\cdot(h_{11s}-h_{10})}{\eta_{com,SCO_2}} \tag{28}$$

$$\eta_{com,SCO_2} = \frac{h_{11s}-h_{10}}{h_{11}-h_{10}} \tag{29}$$

where the CO_2 mass flow rate of flow 10 is $r\cdot\dot{m}_{SCO_2}$, and $h_{10} = h_9$.

The high-temperature flow 9 undergoes isobaric exothermic (9–1) in the water cooler. The heat released can be computed as [45]:

$$P_{cooler} = (1-r)\cdot\dot{m}_{SCO_2}\cdot(h_9-h_1) \tag{30}$$

The flow 3 that has undergone the first recuperator and the flow 11 compressed by RC converge, and then recover heat from the high-temperature flow 7 by HTR (4–5). The recovered heat can be expressed as [44]:

$$Q_{HTR} = \dot{m}_{SCO_2}\cdot(h_5-h_4) = \dot{m}_{SCO_2}\cdot(h_7-h_8) \tag{31}$$

$$h_4 = (1-r)\cdot h_3 + r\cdot h_{11} \tag{32}$$

$$\varepsilon = \frac{h_7-h_8}{h_7-h_8(T_4,p_8)} \tag{33}$$

where $h_8(T_4,p_8)$ represents calculated based on the assumption that the heat flow 8 reaches the temperature T_4 after leaving LTR [44].

CO_2 absorbs heat at isobaric pressure in the heat exchanger (5–6). The outlet flue gas from CC exchanges heat with the CO_2 heated by the recuperators. The heat entering the SCO_2-BC can be denoted as [45]:

$$\dot{m}_{cp}\int_{T_{out2}}^{T_{out1}} C_p(cp)dT = \dot{m}_{SCO_2}\cdot(h_6-h_5) = Q_{in,SCO_2} \tag{34}$$

The heat exchange coefficient of heat exchanger ε_{ex} can be written as [27]:

$$\varepsilon_{ex} = \frac{T_{out1}-T_{out2}}{T_{out1}-T_5} \tag{35}$$

After absorbing heat, CO_2 expands in the turbine (6–7). The output work of the turbine can be expressed as [44,45]:

$$P_T = \dot{m}_{SCO_2}\cdot(h_6-h_{7s})\cdot\eta_{T,SCO_2} \tag{36}$$

$$\eta_{T,SCO_2} = \frac{h_6-h_7}{h_6-h_{7s}} \tag{37}$$

where h_{7s} represents the isentropic enthalpy after turbine outlet; η_{T,SCO_2} is the turbine efficiency, $\eta_{T,SCO_2} = 0.93$ [45,46].

The output power of the SCO_2-BC P_{el,SCO_2} can be expressed as [45]:

$$P_{el,SCO_2} = P_T - P_{MC} - P_{RC} \tag{38}$$

The efficiency of the SCO_2-BC η_{SCO_2} can be defined as [45]:

$$\eta_{SCO_2} = \frac{P_{el,SCO_2}}{Q_{in,SCO_2}} \tag{39}$$

3.5. Simulation of the Cu-Cl cycle

The Cu-Cl cycle in this study includes four basic steps: hydrolysis, thermolysis, electrolysis and drying process. Table 1 lists the corresponding chemical reactions, and it is shown that the products of certain reactions serve as reactants for the subsequent processes. The overall reaction can be expressed as:

$$2H_2O(g) \xrightarrow{\text{Heat and electricity}} 2H_2(g) + O_2(g)$$

Based on the thermal and mass balance, a detailed simulation was performed in Aspen Plus V11, and the detailed flowsheet is shown in Fig. 3 (based on the model developed in Ref. [47]). During the simulation, it was assumed that the reactions realize thermodynamic equilibrium. The models for the hydrolysis and thermolysis reactors were RStoic, while the model of the electrolysis reactor was RGibbs [49]. The property method was the SOLIDS method [48]. Except for the additional thermodynamic data (as shown in Table 2), all other thermodynamic data were taken from the Aspen Plus V11 database.

To recycle the heat released in the cycle as much as possible, a heat recovery device was added to the original process flow, thus the process flow was further optimized (shown in Fig. 4). The model of the heat recovery device is MHeatX. Table 3 provides the energy balance equations of each module.

The output power of the entire system $P_{el,sys}$ is computed as:

$$P_{el,sys} = P_{el,TPV} + P_{el,SCO_2} - P_{el,Cu-Cl} \tag{40}$$

where $P_{el,Cu-Cl}$ denotes electricity required of the Cu-Cl cycle.

The secondary energy efficiency $\eta_{sec,sys}$ of the overall system is defined as [51]:

$$\eta_{sec,sys} = \frac{P_{el,sys}+P_{H_2}}{P_{in}} = \frac{P_{el,sys}+\dot{n}_{H_2}\cdot LHV(H_2)}{P_{in}} \tag{41}$$

Table 1
Reactions of the Cu-Cl cycle at 1 bar [47,48].

Step	Chemical reaction equation	Temperature (°C)	Reaction type
Hydrolysis	$2CuCl_2(s) + H_2O(g) \rightarrow 2HCl(g) + Cu_2OCl_2(s)$	400	Endothermic
Thermolysis	$Cu_2OCl_2(s) \rightarrow 2CuCl(l) + 0.5O_2(g)$	530	Endothermic
Electrolysis	$2CuCl(aq) + 2HCl(g) \rightarrow H_2(g) + 2CuCl_2(aq)$	25	Electrolysis
Drying	$CuCl_2(aq) \rightarrow H_2O(g) + CuCl_2(s)$	130	Endothermic

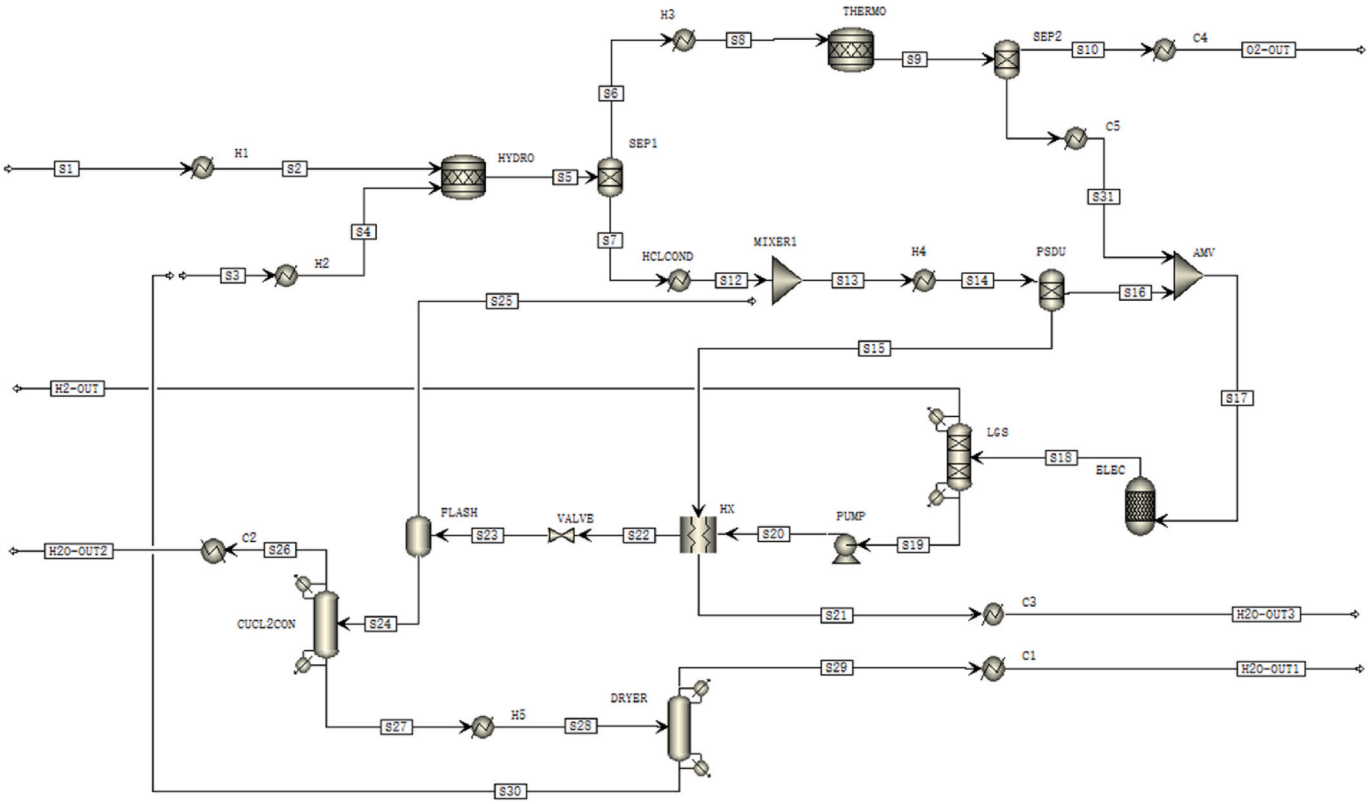

Fig. 3. The detailed flowsheet of the Cu-Cl cycle.

Table 2
Additional thermodynamic data used in the simulation [50].

Compound	DHSFRM (kJ/mol)	DGSFRM (kJ/mol)
$CuCl_2$(s)	−217.4	−173.6
CuCl(s)	−137.0	−120.0
Cu_2OCl_2(s)	−381.3	−310.45

DHSFRM: The formation enthalpy at 25 °C and 1 bar.
DGSFRM: Gibbs free energy of formation at 25 °C and 1 bar.

where $\dot{n}_{H_2}$(mol/s) is the hydrogen production of the Cu-Cl cycle; $LHV(H_2)$ is the lower heating value of H_2, $LHV(H_2) = 241.8$ kJ/mol [22].

The equivalent electrical efficiency $\eta_{el,sys}$ of the system can be defined as:

$$\eta_{el,sys} = \frac{P_{el,sys} + P_{el,H_2}}{P_{in}} = \frac{P_{el,sys} + \dot{n}_{H_2} \cdot LHV(H_2) \cdot \eta_{H-ele}}{P_{in}} \tag{42}$$

where P_{el,H_2}(kW) denotes electricity power converted by H_2; η_{H-ele} represents hydrogen-electricity conversion efficiency, and the specific value is related to the actual process, the power generation efficiency of hydrogen fuel cell is generally in the range of 40–60 % [52], which is taken as 50 % here.

Following the above model description of the overall system, the physical models of solar collector, CC, TPV and SCO_2-BC were programmed with Fortran code, and the Cu-Cl cycle was simulated in Aspen Plus V11. Then, they were coupled to form a complete energy cascade utilization system with solar-gas complementary according to the energy balance, achieving maximum energy utilization. Table 4 lists the input parameters of the simulation. Among them, parameters such as concentration ratio (C) will be regarded as the main research parameters in the parametric analysis. Therefore, the values in Table 4 are represented as a range, and further restrictions and explanations will be made according to the specific research content in the subsequent analysis. The parameter effect was investigated. The calculation flow chart of the overall integrated system simulation is presented in Appendix.

3.6. Exergy destruction models

For the exergy analysis in this study, were ignored, the total exergy of various substances were expressed as the sum of physical and chemical exergy by ignoring the changes in kinetics and potential energy [27]:

$$\dot{E}x = \dot{E}x_{ph} + \dot{E}x_{ch} \tag{43}$$

The exergy of solar energy input $\dot{E}x_{P_{sol}}$ can be calculated as [53]:

$$\dot{E}x_{P_{sol}} = A_d I_s \left[1 + \frac{1}{3}\left(\frac{T_0}{T_{sun}}\right)^4 - \frac{4}{3}\left(\frac{T_0}{T_{sun}}\right)\right] \tag{44}$$

where A_d is the concentrator area; T_{sun} imply to the sun temperature (5800 K).

The physical exergy of air and flue gas is written by Ref. [27]:

$$\dot{E}x_{ph} = \dot{m}[(h - h_0) - T_0(s - s_0)] \tag{45}$$

The chemical exergies of the working fluid (air, flue gas and CO_2) won't change, so it is not considered here. The chemical exergy of fuel and hydrogen is expressed by the following formula:

$$\dot{E}x_{ch,i} = \dot{m}_i Ex_{ch,i} \tag{46}$$

where $Ex_{ch,i}$ is the chemical exergy of fuel or hydrogen ($i = CH_4, H_2$), Ex_{ch,H_2} is taken as 236.09 kJ/mol, Ex_{ch,CH_4} is taken as 831.7 kJ/mol [54].

The exergy balance formulas of each component are illustrated in Table 5, and the exergy destruction and exergy efficiency of each module are illustrated in Table 6, respectively. The exergy destruction factor φ_j of each module is defined as [27]:

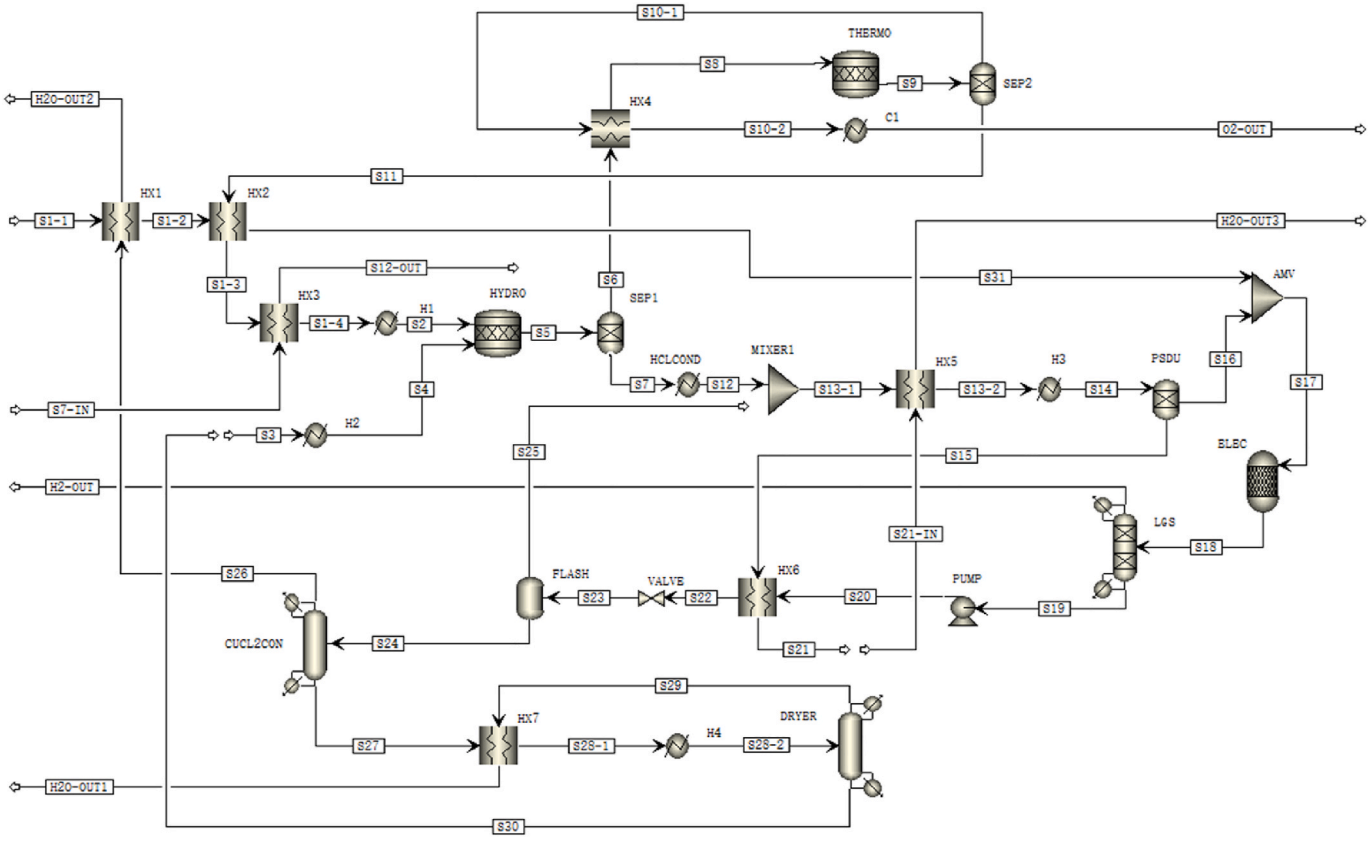

Fig. 4. The detailed flowsheet of the Cu-Cl cycle (containing heat recovery devices).

Table 3
Energy balance formulas for each component of the Cu-Cl cycle based on Fig. 4.

Component	Energy balance formula
Hydrolysis reactor	$\dot{m}_1 h_1 + \dot{m}_3 h_3 + Q_{\text{in,H1}} + Q_{\text{in,H2}} + Q_{\text{heat,Hyd}} = \dot{m}_5 h_5$
Thermolysis reactor	$\dot{m}_8 h_8 + Q_{\text{heat,Ther}} = \dot{m}_9 h_9$
Cooler 1	$\dot{m}_{10-\text{out}} h_{10-\text{out}} = Q_{\text{out,C1}} + \dot{m}_{O_2-\text{out}} h_{O_2-\text{out}}$
PSDU	$\dot{m}_{13-3} h_{13-3} + Q_{\text{in,H3}} = \dot{m}_{15} h_{15} + \dot{m}_{16} h_{16}$
Electrolysis reactor	$\dot{m}_{17} h_{17} + Q_{\text{ele,E}} = \dot{m}_{18} h_{18}$
LGS	$\dot{m}_{18} h_{18} = \dot{m}_{19} h_{19} + \dot{m}_{H_2-\text{out}} h_{H_2-\text{out}}$
Pump	$\dot{m}_{19} h_{19} + Q_{\text{ele,P}} = \dot{m}_{20} h_{20}$
Valve	$\dot{m}_{22} h_{22} = \dot{m}_{23} h_{23}$
Dryer	$\dot{m}_{28-1} h_{28-1} + Q_{\text{in,H4}} = \dot{m}_{29} h_{29} + \dot{m}_{30} h_{30}$

$$\varphi_j = \frac{\dot{E}_j^D}{\dot{E}x_{P_{\text{sol}}} + \dot{E}x_{\text{fuel}}} \tag{47}$$

where $\dot{E}_j^D$ is the exergy destruction of each module ($j = \text{TRs,TPVs,SCO}_2\text{,}$ $\text{Cu}-\text{Cl}$); $\dot{E}x_{\text{fuel}}$ is the exergy of input fuel, $\dot{E}x_{\text{fuel}} = \dot{E}x_{\text{ch,CH}_4}$ in this paper.

4. Results and discussion

4.1. Model validation

The SCO_2-BC studied in this study is based on the model developed by Xu [45] and Sun [46]. They both studied a SCO_2 recompression cycle with two recuperators. In the cycle, SCO_2 was split and entered the main-compressor and the re-compressor, respectively. This structure is consistent with that of SCO_2-BC simulated in this study. Comparing the current results with those of previous studies, it shows that the results are in good agreement with the references as shown in Table 7 when the parameter settings of SCO_2-BC in this study are consistent with those reported in the references, the present model efficiency differs from the results of the references by less than 1 %, which indicates that the SCO_2-BC model selected is reasonable. The specific thermodynamic data of each flow are shown in Table 8. In the SCO_2-BC, the split flow 3 and

Table 4
Input parameter of the simulation of the proposed system.

Module	Parameter	Value
Solar collector	Concentration ratio C	100–800
	Tube receiver area S_1 (m^2)	0.005–0.02
CC	Fuel input power P_{fuel} (kW)	15
	Fuel type	CH_4
	Lower heating value of fuel (kJ/kg)	50016 [37]
	Excess air coefficient	1.1
	Oxygen ratio R_{O_2}	0.21–0.35
	Surface heat transfer coefficient H (W/(m^2·K))	100 [12]
	Combustion chamber area/TPV area S_2 (m^2)	0.5–5.0
	Emissivity of the emitter ε_{em}	0.9 [39]
	Ratio of the luminous particles m_{lu}	0.1 [39]
	Emissivity of the luminous particles ε_{lu}	0.85 [39]
TPV	PV cell type	GaAs
	Band gap of the PV cell (eV)	1.42 [42]
	Cut-off wavelength of the filter (nm)	950 [42]
SCO_2-BC	Turbine inlet temperature T_6 (K)	950–1125
	Compressor inlet temperature T_{com} (K)	305.15 [45,46]
	Maximum pressure p_{max} (MPa)	25 [45,46]
	Minimum pressure p_{min} (MPa)	7.38 [45,46]
	Compressor efficiency $\eta_{\text{com,SCO}_2}$	0.89 [45,46]
	Turbine efficiency $\eta_{\text{T,SCO}_2}$	0.93 [45,46]
	Recuperator efficiency ε	0.95 [45]
	The heat exchange coefficients of heat exchanger ε_{ex}	0.85
Cu-Cl cycle	Mass flow rate of water input (kg/s)	1.0000
	H_2O/Cu ratio	12 [47]

Table 5
Exergy balance formulas of each component.

Component	Exergy balance formula
Concentrator	$\dot{E}_{C}^{D} = \dot{E}x_{P_{sol}} - \dot{E}x_{P_1}$
Tube receiver	$\dot{E}_{TR}^{D} = \dot{E}x_{P_1} + \dot{E}x_{T_0} - \dot{E}x_{T_{air}}$
CC	$\dot{E}_{CC}^{D} = \dot{E}x_{T_{air}} + \dot{E}x_{fuel} - \dot{E}x_{af}$
TPV	$\dot{E}_{TPV}^{D} = \dot{E}x_{af} - \dot{E}x_{T_{out1}} - P_{el,TPV}$
Heat exchanger	$\dot{E}_{HX}^{D} = \dot{E}x_{T_{out1}} + \dot{E}x_5 - \dot{E}x_{T_{out2}} - \dot{E}x_6$
Turbine	$\dot{E}_{T}^{D} = \dot{E}x_6 - \dot{E}x_7 - P_T$
HTR	$\dot{E}_{HTR}^{D} = \dot{E}x_7 + \dot{E}x_4 - \dot{E}x_8 - \dot{E}x_5$
LTR	$\dot{E}_{LTR}^{D} = \dot{E}x_8 + \dot{E}x_2 - \dot{E}x_9 - \dot{E}x_3$
MC	$\dot{E}_{MC}^{D} = P_{MC} + \dot{E}x_1 - \dot{E}x_2$
RC	$\dot{E}_{RC}^{D} = P_{RC} + \dot{E}x_{10} - \dot{E}x_{11}$
Thermolysis	$\dot{E}_{the}^{D} = \dot{E}x_{T_{out2}} + \dot{E}x_{Cu_2OCl_2} - \dot{E}x_{O_2} - \dot{E}x_{CuCl} - \dot{E}x_{T_{out3}}$
Hydrolysis	$\dot{E}_{hyd}^{D} = \dot{E}x_{T_{out3}} + \dot{E}x_{H_2O} + \dot{E}x_{CuCl_2} - \dot{E}x_{Cu_2OCl_2} - \dot{E}x_{HCl} - \dot{E}x_{T_{out4}}$
Dryer	$\dot{E}_{dry}^{D} = \dot{E}x_{T_{out4}} + \dot{E}x_{CuCl_2(aq)} - \dot{E}x_{CuCl_2} - \dot{E}x_{T_{out5}}$
Electrolysis	$\dot{E}_{ele}^{D} = P_{el,Cu-Cl} + \dot{E}x_{HCl} - \dot{E}x_{CuCl} - \dot{E}x_{CuCl_2(aq)} - \dot{E}x_{H_2}$

Table 6
Exergy destruction and exergy efficiency formulas of each module.

Module	Exergy destruction	Exergy efficiency
Tube receiver (include concentrator)	$\dot{E}_{TRs}^{D} = \dot{E}_{C}^{D} + \dot{E}_{TR}^{D}$	$\eta_{ex,TRs} = \frac{\dot{E}x_{T_{air}} - \dot{E}x_{T_0}}{\dot{E}x_{P_{sol}}}$
TPV (include CC)	$\dot{E}_{TPVs}^{D} = \dot{E}_{CC}^{D} + \dot{E}_{TPV}^{D}$	$\eta_{ex,TPVs} = \frac{P_{el,TPV}}{\dot{E}x_{T_{air}} + \dot{E}x_{fuel} - \dot{E}x_{T_{out1}}}$
SCO_2-BC	$\dot{E}_{SCO_2}^{D} = \dot{E}_{HX}^{D} + \dot{E}_{T}^{D} + \dot{E}_{HTR}^{D} + \dot{E}_{LTR}^{D} + \dot{E}_{MC}^{D} + \dot{E}_{RC}^{D}$	$\eta_{ex,SCO_2} = \frac{P_T - P_{MC} - P_{RC}}{\dot{E}x_{T_{out1}} - \dot{E}x_{T_{out2}}}$
Cu-Cl	$\dot{E}_{Cu-Cl}^{D} = \dot{E}_{the}^{D} + \dot{E}_{hyd}^{D} + \dot{E}_{dry}^{D} + \dot{E}_{ele}^{D}$	$\eta_{ex,Cu-Cl} = \frac{\dot{E}x_{H_2}}{\dot{E}x_{T_{out2}} - \dot{E}x_{T_{out5}} + P_{el,Cu-Cl} + \dot{E}x_{H_2O}}$

Table 7
Comparison results with previous study of the SCO_2-BC.

Parameter	Present model	Reference [45]	Reference [46]
Turbine inlet temperature T_6 (°C)	850	850	850
Compressor inlet temperature T_{com} (°C)	32	32	32
Maximum pressure p_{max} (MPa)	25	25	25
Minimum pressure p_{min} (MPa)	7.38	7.38	7.38
Compressor efficiency η_{com,SCO_2}	0.89	0.89	0.89
Turbine efficiency η_{T,SCO_2}	0.93	0.93	0.93
Recuperator efficiency ε	0.95	–	0.95
Pressure drops in heat exchangers (MPa)	–	0.13	–
Split ratio r	0.224	–	–
Overall efficiency	57.0 %	56.7 %	58 %

split flow 11 converge into flow 4 (as shown in Fig. 1). The efficiency of the cycle will be the highest when the two flows have the same temperature before converging. Then the optimal r of the SCO_2-BC can be calculated. Unless otherwise specified, the split ratio refers to the optimal one in this paper.

The Cu-Cl cycle studied in this paper is based on the model developed by Zhang [47] and Orhan [49]. They both simulated the detailed process flow of the four-step Cu-Cl cycle using Aspen Plus (without heat recovery devices inside the cycle). This structure is basically consistent with that of Cu-Cl cycle simulated in this study. The H_2O/Cu ratio was set as 12. The thermodynamic data of each stream are illustrated in Table 9. The results are consistent with that reported in Ref. [47]. There are great amounts of heating and cooling processes in the Cu-Cl cycle.

Table 8
Thermodynamic data of each flow of the SCO_2-BC.

Flow	Temperature (°C)	Pressure (MPa)	h (J/mol)
1	32	7.38	16756.43
2	109.48	25	18700.77
3	245.59	25	28466.96
4	245.50	25	28461.77
5	619.64	25	49268.22
6	850	25	62258.40
7	669.23	7.38	52398.04
8	267.70	7.38	31591.59
9	116.81	7.38	24013.03
10	116.81	7.38	24013.03
11	245.20	25	28443.80

Based on the formulas in Table 3 and the data in Table 9, the energy requirement of each step can be calculated, and the results are presented in Table 10 (endothermic processes are expressed as positive, exothermic processes are expressed as negative). The comparison results with previous study of the Cu-Cl cycle are detailed in Table 11. Since Ref. [49] considers the heat required in drying process as the electricity required, there is a gap between its energy demands and those of present model. However, the results are still reasonable, indicating that the Cu-Cl cycle model selected in this study is reasonable.

The exergy analysis model selected in this study is a typical exergy analysis method, which has been reported in some literatures [27,55]. We selected a typical dynamic cycle for verification. Salim et al. [56] studied a recompression SCO_2-BC with a two-stage compressor and a two-stage recuperator. When the main-compressor inlet pressure is 7.8 MPa, the main-compressor outlet pressure is 24 MPa, the turbine inlet temperature is 700 °C and the split ratio (the proportion of the working fluid flow entering the main-compressor to the total flow) is 0.74, the exergy efficiency of SCO_2-BC is 74.20 %. When the parameter settings are consistent with those in Ref. [56], the calculated exergy efficiency of SCO_2-BC is 72.87 % using the exergy analysis model of this study, which are in good agreement with the results reported in Ref. [56]. This indicates that the exergy analysis model selected in this study is reasonable.

4.2. Effect of system parameters on the performance of TPV module

Since selecting system parameters reasonably is crucial to the system operation, the safety, economy and effectiveness should be comprehensively considered. As shown in Fig. 5, the outlet air temperature T_{air} rises with the concentration ratio C under different tube receiver areas S_1. The larger S_1 is, the faster T_{air} increases, revealing that more energy enters the TPV module. The upper limit of the air preheating temperature cannot be ignored when designing the solar collector in actual engineering applications. For a tube receiver, the temperature of its working fluid should generally not exceed 1000 K [57], otherwise many safety problems will arise, such as the destruction of the tube receiver caused by working fluid, the destruction of CC caused by the excessively high-temperature flame, and so on. Therefore, a reasonable combination of S_1 and C must be used. That is, the combinations of S_1 and C should be selected when T_{air} is as close as possible to the dotted line (but not exceeding), such as C=300 and S_1=0.015 m^2, C=400 and S_1=0.01 m^2, C=500 and S_1=0.01 m^2 (as shown in Fig. 5).

To ensure the rationality of T_{air}, the performance of the PV cell is investigated when S_1 is 0.005 m^2, 0.01 m^2 and 0.015 m^2, respectively. The TPV area S_2 was set as 3.0 m^2, and C was limited within the range of 100–600. As presented in Fig. 6(a), the emitter wall temperature T_{em} rises with C. When S_1 is 0.015 m^2, the temperature and its increasing amplitude are both the largest (from 1634.8 K to 1710.4 K). This is because the larger S_1 is, the more energy enters the TPV module and the faster T_{em} increases. From Fig. 6(b), it shows that both $P_{el,TPV}$ and η_{cell} increase with C, and their increase amplitude are both the largest when

Table 9
Thermodynamic data of each stream point of Cu-Cl cycle.

Stream	Species	Temperature (°C)	Pressure (bar)	$\dot{m}$ (kg/s)	h (simulated) (kJ/kg)	h (reference) (kJ/kg)
S1-1	H_2O	25	1	1.0000	−15864.3	−15864.3
S1-2	H_2O	27.1	1	1.0000	−15855.6	–
S1-3	H_2O	58.1	1	1.0000	−15726	–
S1-4	H_2O	369.5	1	1.0000	−12753.6	–
S2	H_2O	400	1	1.0000	−12690.9	−12690.9
S3	$CuCl_2$	130	1	0.6000	−1473.59	–
S4	$CuCl_2$	400	1	0.6000	−1318.27	−1318.3
S5	$H_2O/HCl/Cu_2OCl_2$	400	1	1.6000	−8347.5	−8341.5
S6	Cu_2OCl_2	400	1	0.4775	−1701.6	−1681.5
S7	H_2O/HCl	400	1	1.1225	−11174.5	−11175.5
S7-in	H_2O/HCl	400	1	1.1225	−11174.5	−11175.5
S8	Cu_2OCl_2	530	1	0.4775	−1673.81	−1653.7
S9	$O_2/CuCl$	530	1	0.4775	−981.62	−981.6
S10-1	O_2	530	1	0.0357	498.04	498.0
S10-2	O_2	160.6	1	0.0357	126.3	–
S11	CuCl	530	1	0.4418	−1101.19	−1101.2
S12	H_2O/HCl	50	1	1.1225	−13823	−13825.20
S12-out	H_2O/HCl	50	1	1.1225	−13823	−13825.20
S13-1	H_2O/HCl	50	1	1.1225	−13823	−13825.20
S13-2	H_2O/HCl	97.3	1	1.1225	−11887.2	–
S14	H_2O/HCl	106	1	1.1225	−11704.9	−11707.70
S15	H_2O	106	1	0.8600	−13271	−13274.09
S16	H_2O/HCl	106	1	0.2625	−6574.5	−6576.49
S17	$H_2O/HCl/CuCl$	83.7	1	0.7043	−3325.33	–
S18	$H_2O/CuCl_2/H_2$	25	1	0.7043	−3545.86	−3548.25
S19	$H_2O/CuCl_2$	25	1	0.6998	−3575.18	−3575.69
S20	$H_2O/CuCl_2$	25	2	0.6998	−3575.16	−3575.62
S21	H_2O	100	1	0.8600	−13337.6	−13340.7
S21-in	H_2O	100	1	0.8600	−13337.6	−13340.7
S22	$H_2O/CuCl_2$	102	2	0.6998	−3493.22	−3493.77
S23	$H_2O/CuCl_2$	60	0.2	0.6998	−3493.22	−3493.77
S24	$H_2O/CuCl_2$	60	0.2	0.6866	−3303.25	−3302.86
S25	H_2O	60	0.2	0.0132	−13357.4	−13358.26
S26	H_2O	60	0.2	0.0592	−13357.4	−13358.26
S27	$H_2O/CuCl_2$	60	0.2	0.6274	−2131.79	−2131.36
S28-1	$H_2O/CuCl_2$	80.4	0.2	0.6274	−2016.53	–
S28-2	$H_2O/CuCl_2$	130	1	0.6274	−1986.02	−1985.94
S29	H_2O	130	1	0.0274	−13225.4	−13228.27
S30	$CuCl_2$	130	1	0.6000	−1473.59	−1473.59
S31	CuCl	25	1	0.4418	−1394.66	−1394.66
H_2O-out1	H_2O	25	1	0.0357	−15864.3	−15864.3
H_2O-out2	H_2O	25	1	0.0592	−15864.3	−15864.3
H_2O-out3	H_2O	25	1	0.86	−15864.3	−15864.3
O_2-out	O_2	25	1	0.0274	−1.16420E-13	–
H_2-out	H_2	25	1	0.0045	1.84797E-12	–

Table 10
Energy requirement of each step in Cu-Cl cycle.

Component	Process	Heat required kJ/(mol H_2)	Electricity required kJ/(mol H_2)
Hydrolysis reactor	$CuCl_2(s)/H_2O(g) \xrightarrow{400^\circ C} HCl(g)/Cu_2OCl_2(s)$	+55.92	–
Thermolysis reactor	$Cu_2OCl_2(s) \xrightarrow{530^\circ C} CuCl(l)/O_2(g)$	+146.90	–
Electrolysis reactor	$CuCl(aq)/HCl(g) \xrightarrow{25^\circ C} H_2(g)/CuCl_2(aq)$	–	55
Dryer	$CuCl_2(aq) \xrightarrow{130^\circ C} H_2O(g)/CuCl_2(s)$	–	–
Heater 1	$H_2O(369.5^\circ C) \rightarrow H_2O(400^\circ C)$	+27.88	–
Heater 2	$CuCl_2(130^\circ C) \rightarrow CuCl_2(400^\circ C)$	+40.97	–
Heater 3	$HCl/H_2O(97.3^\circ C) \rightarrow HCl/H_2O(106^\circ C)$	+69.80	–
Heater 4	$H_2O/CuCl_2(80.4^\circ C) \rightarrow H_2O/CuCl_2(130^\circ C)$	+8.48	
Pump	Pump the solution to the heat exchanger	–	2.76
Cooler 1	$O_2(160.6^\circ C) \rightarrow O_2(25^\circ C)$	−2.00	–

S_1 is 0.015 m^2 ($P_{el,TPV}$ increases from 6.32 kW to 10.55 kW, η_{cell} increases from 67.32 % to 67.61 %). This is because a higher T_{em} means more output radiation power and higher cell efficiency, and the effect became more significant when S_1 is large. The increase of $P_{el,TPV}$ with C is almost linear, which is basically consistent with the T_{em} trend. Furthermore, when S_1 is 0.015 m^2, η_{cell} increases slowly after C is greater than 200; while this critical C became 300, and 400 when S_1 is 0.01 m^2 and 0.005 m^2, respectively. Indeed, it is uneconomical to choose an excessively large C. When S_1 is large, there might be safety problems caused by the excessively high preheated air temperature; However, even if the requirements of safety and economy can be met when S_1 is too small, the $P_{el,TPV}$ will be extremely low simultaneously. It is essential to comprehensively consider safety, economy and efficiency in selecting the appropriate combination of S_1 and C.

TPV area S_2 means the emitter area, determines the amount of radiation energy from CC, thus affects $P_{el,TPV}$ and η_{cell}. It is also essential to choose a suitable S_2, After the preliminary analysis, S_1=0.01 m^2 and C=400 were selected for further research. As presented in Fig. 7(a), the

Table 11
Comparison results with previous study of the Cu-Cl cycle.

Parameter	Present model	Reference [47]	Reference [49]
Hydrolysis reaction temperature (°C)	530	530	500
Thermolysis reaction temperature (°C)	400	400	400
Electrolysis reaction temperature (°C)	25	25	25
Drying reaction temperature (°C)	130	130	80
Net heat required (kJ/(mol H_2))	349.95	338.26	353.8
Net electricity required (kJ/(mol H_2))	57.76	57.76	96.2
Overall efficiency	59.30 %	61.06 %	50.40 %

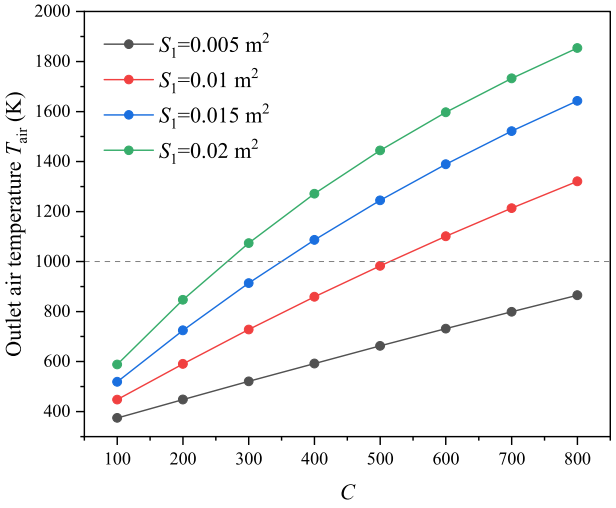

Fig. 5. Influence of concentration ratio (C) on air temperature at solar collector outlet for different tube receiver areas (S_1).

emitter wall temperature T_{em} (from 1919.0 K to 1601.8 K) and the TPV outlet flue gas temperature T_{out1} (from 1569.4 K to 1125.5 K) decrease with the increase of S_2, and the decreasing trends becomes slowly with S_2. According to the thermal balance of CC, more energy passes through the emitter with the increase of S_2, which causing the reduction of T_{em}. As shown in Fig. 7(b), $P_{el,TPV}$ increases from 5.72 kW to 8.39 kW with S_2, nevertheless it shows a gradual downward trend. Additionally, η_{cell} increased with S_2 (from 65.62 % to 67.89 %), which is similar to the trend of $P_{el,TPV}$. It is illustrated that blindly increasing S_2 is uneconomical. Besides, it can be found that when S_2=5 m^2, T_{out1}=1125.5 K, and if S_2 is further increased, it will inevitably lead to T_{out1}<1125 K. From the perspective of the system, according to the second law of thermodynamics, the requirement of 1125 K for the SCO_2-BC turbine inlet temperature cannot be met. This is also the key reason why S_2 cannot be blindly increased. Out of reasonable considerations, S_2 should not exceed 4.0 m^2 (T_{out1}=1159.19 K), and S_2=3.0 m^2 is a reasonable, efficient and economical choice (T_{out1}=1205.12 K). From the perspective of the TPV module, for fixed S_1 and C, the larger S_2 means a greater $P_{el,TPV}$ and a lower T_{out1}. That is, more energy is utilized in TPV and the heat contained in the outlet flue gas is reduced. At the same time, there is less energy for the modules of SCO_2-BC and Cu-Cl cycle, leading to the reduction of the output power of subsequent modules. Consequently, it is necessary to synergistically discuss with the parameters of subsequent modules for comprehensive analysis of the entire system.

4.3. Effect of system parameters on the performance of integrated system

According to section 4.2, the combination of S_1 and C determines the total solar energy that system harvesting. When S_1 and C is fixed, S_2 determines $P_{el,TPV}$ and T_{out1}, implying that S_2 determines the energy distribution between TPV module and the subsequent modules (the total energy input maintains). Similarly, the turbine inlet temperature (T_6) usually determines the output power and efficiency of the SCO_2-BC, and also affects the energy entering the Cu-Cl module. Indeed, it's essential to analyze the effect of these parameters on the entire system.

The extremely small temperature difference between T_{out1} and T_6 poses a significant challenge to heat exchange. Therefore, when T_6=1125 K is to be satisfied, S_2 should not exceed 4.0 m^2, and S_2=3.0 m^2 is a reasonable, efficient and economical choice. Since the specific temperature requirements of the Cu-Cl cycle (as presented in Table 1), the reaction temperature required for each step must be taken into consideration in analyzing. As shown in Table 9 and Fig. 2, the temperature of various module outlet flue gas must satisfy T_{out2}≥803 K, T_{out3}≥673 K, and T_{out4}≥403 K. After calculation and analysis, it can be found that T_6≥950 K must be satisfied, otherwise T_{out2} will be lower than 803 K, meaning that the reaction temperature requirements of the Cu-Cl cycle won't be met. Under the optimal split ratio, a higher T_6 means a greater SCO_2-BC efficiency [44], but considering the long-term stability and reliability of the material [58], it is not advisable to set T_6 too high. Therefore, T_6 is limited to the range of 950–1125 K in this study. When coupling the Cu-Cl cycle, the waste heat recovered from the PV water cooler can be used to preheat the reactants (mainly water) in the Cu-Cl cycle (as presented in Fig. 2).

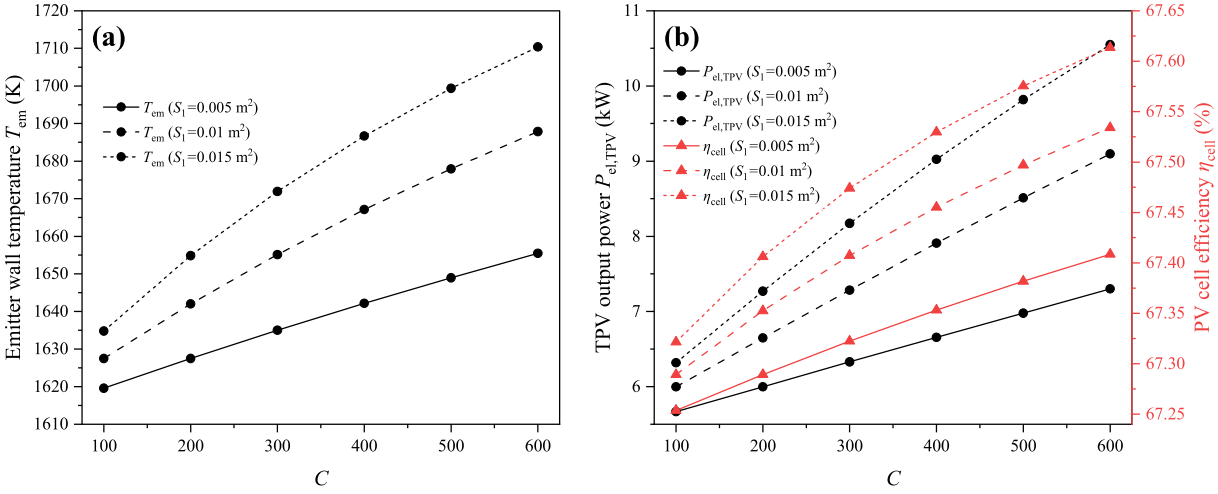

Fig. 6. Influence of the concentration ratio (C) on the power generation performance under different receiver area (S_1): (a) the emitter wall temperature; (b) the TPV output power and PV cell efficiency.

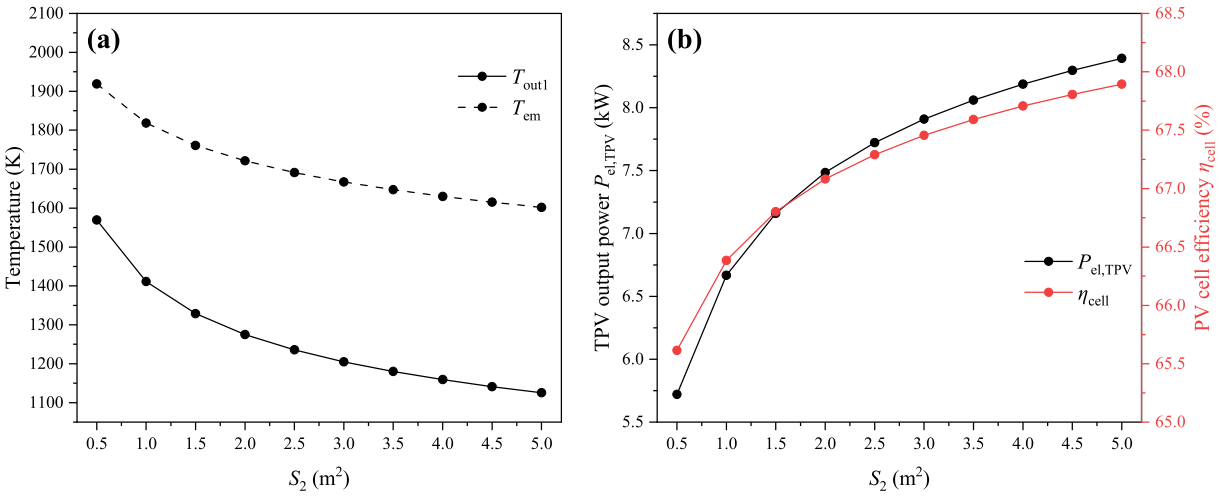

Fig. 7. Effect of TPV areas (S_2) on TPV module: (a) different types of temperature; (b) TPV output power and PV cell efficiency.

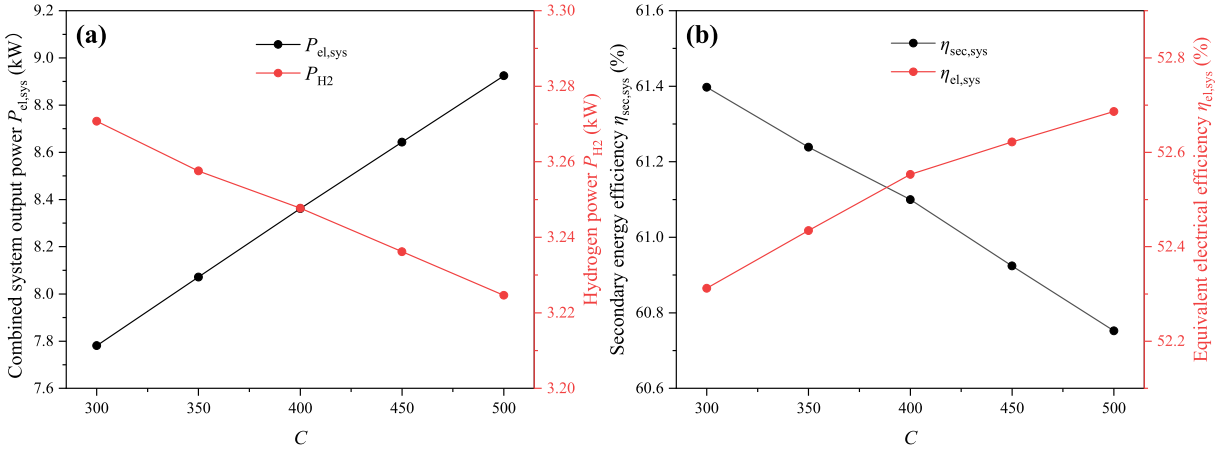

Fig. 8. Effect of concentrate ratio (C) on integrated system: (a) output power and hydrogen power; (b) secondary energy efficiency and equivalent electrical efficiency.

Following the analysis of TPV module and SCO_2-BC module, the working condition of S_1=0.01 m^2, S_2=3.0 m^2, T_6=1125 K were selected to explored the effect of C on the integrated system. Fig. 8 shows the relationships between C (300–500) and the system output power $P_{el,sys}$ (Eq. (40)), hydrogen power P_{H2} and efficiency. As shown in Fig. 8(a), when C increases, $P_{el,sys}$ increases (from 7.78 kW to 8.92 kW) while P_{H2} decreases slightly (from 3.27 kW to 3.22 kW). This is because more solar energy enter the system with the increase of C, the air will be preheated and the emitter temperature T_{em} will also be higher, resulting in a significant increase in TPV power generation. However, T_6 remains constant represents that the medium-temperature energy is almost unchanged and the energy allocated to Cu-Cl module is almost

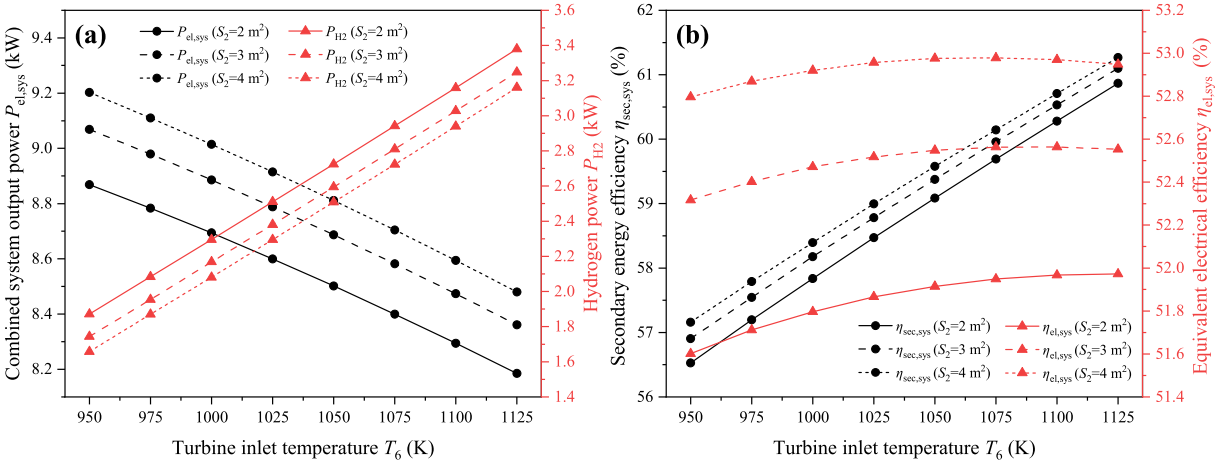

Fig. 9. Effect of turbine inlet temperature (T_6) on integrated system: (a) output power and hydrogen power in different TPV areas (S_2); (b) secondary energy efficiency and equivalent electrical efficiency in different TPV areas (S_2).

unchanged as well, thus the production of H_2 changes slightly. It should be noted that the hydrogen production has decreased slightly with C. This is because the energy entering the SCO_2-BC module also increases slightly when C increases while T_6 remains, leading to the decrease of T_{out2}. Therefore, the energy that can be effectively utilized by Cu-Cl cycle decreases, and P_{H2} decreases slightly. As presented in Fig. 8(b), the secondary energy efficiency $\eta_{sec,sys}$ decreases slightly (from 61.40 % to 60.75 %) with C, and the equivalent electrical efficiency $\eta_{el,sys}$ increases from 52.31 % to 52.69 %. This is because the proportion of energy in the high-temperature section increases with C, leading to an increase in the proportion of electrical energy production. It is indicated that C can be a parameter for the system to adjust the ratio of electricity/hydrogen production.

Fig. 9 shows the effect of T_6 (950–1125 K) on the output power, hydrogen power and efficiency of integrated system under different S_2 (2.0–4.0 m^2). The working conditions of S_1=0.01 m^2 and C=400 were set. From Fig. 9(a), it can be observed that $P_{el,sys}$ decreases with T_6. When S_2 is 2.0 m^2, $P_{el,sys}$ is reduced from 8.87 kW to 8.18 kW; when S_2 is 4.0 m^2, $P_{el,sys}$ is reduced from 9.20 kW to 8.48 kW. In contrast, the P_{H2} increases with T_6, and the hydrogen power curve moves downward as S_2 increases. When S_2 is 2.0 m^2, the P_{H2} increases from 1.87 kW to 3.38 kW; when S_2 is 4.0 m^2, the P_{H2} increases from 1.66 kW to 3.16 kW. This is because when S_2 remains constant, the total energy entering the SCO_2-BC module and the Cu-Cl module is kept. Currently, a higher T_6 means a greater outlet flue gas temperature T_{out2}, that is, the less energy entering the SCO_2-BC module, leading to the reduction of output power. Meanwhile, the energy entering the Cu-Cl module increases, implying more energy can be efficiently cascade utilized by the Cu-Cl cycle. Hence P_{H2} increases, while $P_{el,sys}$ is further reduced since the electricity consumed by hydrogen production increases. Moreover, it shows that as S_2 increases, the $P_{el,sys}$ curve moves upward, while the P_{H2} curve moves downward. This is because when S_2 increases and T_6 remains constant, the total energy entering the subsequent modules (SCO_2-BC, Cu-Cl cycle) decreases while the energy distribution remains unchanged, leading the reduction of P_{H2}. Therefore, the energy entering the TPV module increases, and the energy entering the SCO_2-BC module decreases. Due to the efficiency of the TPV cell is greater than that of the SCO_2-BC, $P_{el,sys}$ increases with the increase of S_2. From Fig. 9(b), it shows that the secondary energy efficiency $\eta_{sec,sys}$ increases with T_6. When S_2 is 2.0 m^2, $\eta_{sec,sys}$ increases from 56.53 % to 60.86 %; when S_2 is 4.0 m^2, $\eta_{sec,sys}$ increases from 57.16 % to 61.26 %. The equivalent electrical efficiency $\eta_{el,sys}$ shows a trend from rising to decline, but the overall variation is very slight. When S_2 is 2.0 m^2, $\eta_{el,sys}$ is approximately between 51.60 % and 51.97 %, reaching a peak at T_6=1125 K; when S_2 is 4.0 m^2, $\eta_{el,sys}$ is approximately between 52.87 % and 52.98 %, reaching a peak at T_6=1075 K.

In conclusion, within the range of S_2=2.0–4.0 m^2 and T_6=950–1125 K, when S_1=0.01 m^2, C=400, S_2=4 m^2 and T_6=1125 K, the secondary energy efficiency is the highest ($\eta_{sec,sys}$=61.26 %). When S_1=0.01 m^2, C=400, S_2=4 m^2 and T_6=1075 K, the equivalent electrical efficiency is the highest ($\eta_{el,sys}$=52.98 %). Clearly, it is illustrated that S_2 and T_6 can be parameters for the system to adjust the ratio of electricity/hydrogen production. The smaller S_2 is and the higher T_6 is, the higher the ratio of hydrogen generation is. Furthermore, the S_2 and T_6 have little synergistic effect on the quality of hydrogen-electric energy, and $\eta_{el,sys}$ is above 51 %.

4.4. Effect of oxygen recovery on integrated system

In addition to producing hydrogen, the Cu-Cl cycle also produces an equal oxygen. The oxygen-enriched combustion can be achieved if part of this oxygen is mixed with the inlet air and passed into CC. The flame temperature can be further enhanced, thereby affecting the output power of each module and the system efficiency. In engineering applications, the system device cannot always operate under the conditions of rated solar radiation intensity (such as cloudy days or nights). It's able to maintain the high-efficiency operation of the system device by appropriately increasing the oxygen ratio (R_{O2}), which has engineering significance. Therefore, the effect of oxygen recovery on the system with/without solar input was discussed in this section.

The working conditions of S_1=0.01 m^2, S_2=3.0 m^2, and C=400 were set to explore the effect of oxygen recovery. The calculation showed that the oxygen production of the Cu-Cl cycle can adjust the R_{O2} within the range of 0.21–0.35. In the absence of solar input, the CH_4 content was increased to make the total energy input consistent. As shown in Fig. 10 (a), when R_{O2} increases from 0.21 to 0.35, T_{em} increases but T_{out1} decreases. This is because the increase in R_{O2} can elevate the flame temperature, thereby increasing the energy utilized by TPV module. In the absence of solar preheating, T_{em} is lower than that with solar preheating under the same conditions, but T_{out1} is higher. It reveals that less energy can be efficiently utilized by the TPV module. The primary reason is the lower temperature of inlet oxygen-enriched gas without solar preheating. As presented in Fig. 10(b), when R_{O2} increases, the TPV output power increases from 7.91 kW to 9.86 kW (with solar input) and from 6.50 kW to 9.42 kW (without solar input), the trend is consistent with T_{em}. The SCO_2-BC output power decreases from 1.19 kW to 0.38 kW (with solar input) and from 1.98 kW to 0.76 kW (without solar input) with R_{O2}, and the decreasing trend gradually slows down. This is because there is less inlet gas (the amount of TPV outlet flue gas also decreases) and T_{out1} decreases simultaneously. It suggested that the energy contained in the TPV outlet flue gas decreases, the energy available for the SCO_2-BC and Cu-Cl cycle decrease (as shown in Fig. 10 (c)). In addition, from Fig. 10(c), it shows that the total output power of the integrated system increases from 8.36 kW to 9.80 kW (with solar input) and from 7.71 kW to 9.71 kW (without solar input) with R_{O2}. By combining with Fig. 10(b) and (c), it shows that when there is no solar input, the SCO_2-BC output power and hydrogen power are higher than those with solar input. This is because T_{out1} is higher and there is more inlet oxygen-enriched gas, so the flue gas entering the subsequent stages contains more energy, and can be efficiently utilized. As shown in Fig. 10 (d), as R_{O2} increases from 0.21 to 0.35, the secondary energy efficiency $\eta_{sec,sys}$ of the system increases from 61.10 % to 61.94 % (with solar input) and from 58.44 % to 61.89 % (without solar input), while the equivalent electrical efficiency $\eta_{el,sys}$ increases from 52.55 % to 56.77 % (with solar input) and from 49.52 % to 56.49 % (without solar input). When R_{O2} increases to about 0.29–0.31 without solar input, the same $\eta_{sec,sys}$ can be achieved as that with solar input (R_{O2}=0.21). Furthermore, when it increases to about 0.25–0.27 without solar input, the same $\eta_{el,sys}$ can be achieved as that with solar input (R_{O2}=0.21). It is fully illustrated that adding oxygen recovery to the system can effectively improve the system performance. When there is insufficient solar energy input, the system device is able to operate continuously and efficiently by appropriately increasing R_{O2}.

4.5. Exergy analysis

The effect of typical parameters on the exergy destruction of system key components was investigated in this section, and typical working conditions are selected. Based on the equations in Table 6, the exergy efficiency and exergy destruction factor of different modules were calculated as shown in Figs. 11 and 12, respectively. The exergy efficiency of tube receiver module ($\eta_{ex,TRs}$) maintains 39.46 %, and the exergy destruction factor (φ_{TRs}) maintains 11.68 %, so they are not shown in the figures.

For the purpose of discussing the effect of S_2 on integrated system, the parameters were set as: S_1=0.01 m^2, C=400, T_6=1125 K, and

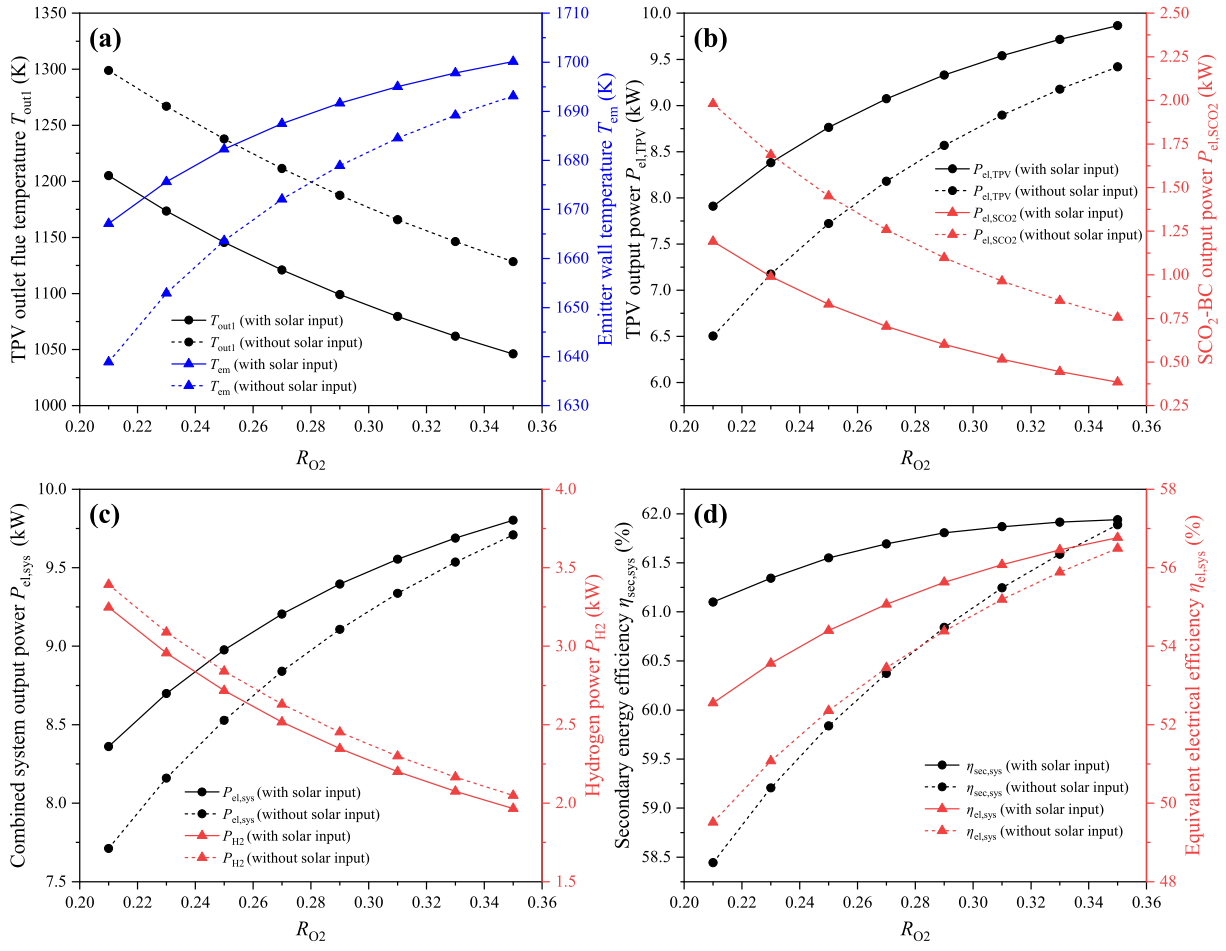

Fig. 10. Effect of oxygen ratio (R_{O2}) on integrated system: (a) different types of temperature; (b) output power of TPV and SCO_2-BC; (c) integrated system output power and hydrogen power; (d) integrated system efficiency.

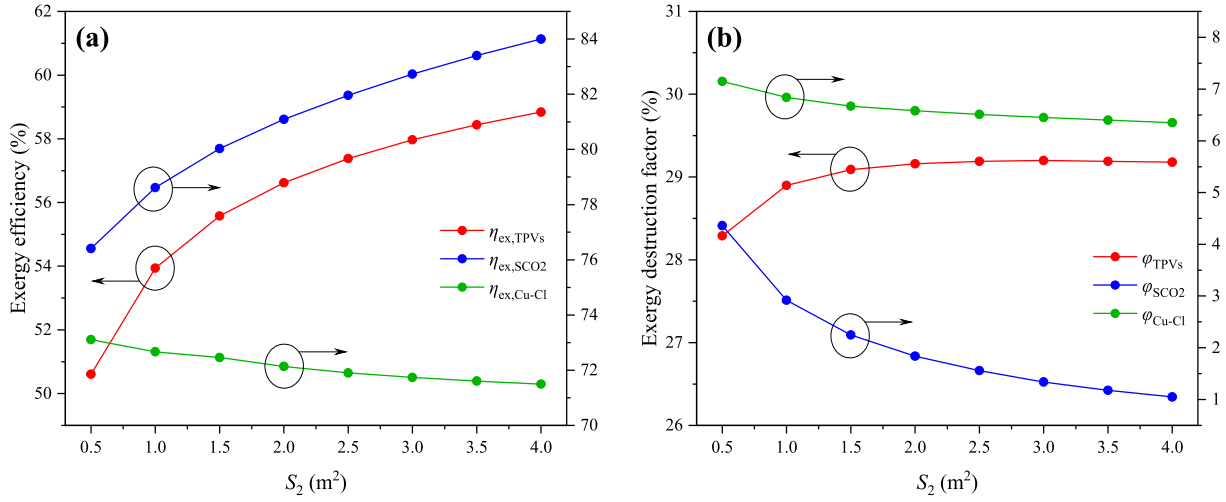

Fig. 11. Effect of TPV area (S_2) on integrated system: (a) exergy efficiency; (b) exergy destruction factor.

R_{O2}=0.21. As shown in Fig. 11, when S_2 increases from 0.5 m^2 to 4.0 m^2, the exergy efficiency of TPV module ($\eta_{ex,TPVs}$) increases from 50.61 % to 58.84 %, and the exergy destruction factor (φ_{TPVs}) increases slightly from 28.29 % to 29.18 %. This is because a greater S_2 means a lower the average temperature in CC, and the exergy value per unit flue gas energy decreases, that is, the denominator for calculating TPV exergy efficiency decreases. Meanwhile, the increase in TPV power generation capacity also enhances the exergy destruction of the TPV module. Besides, the exergy efficiency of SCO_2-BC module (η_{ex,SCO_2}) increases from 76.41 % to 84.00 %, and the exergy destruction factor (φ_{SCO_2}) decreases from 4.36

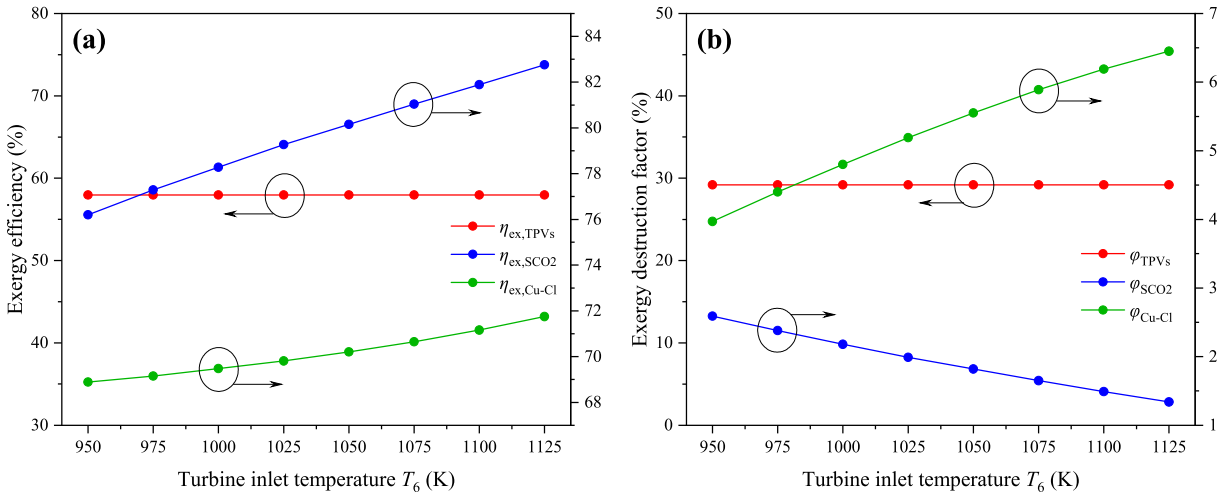

Fig. 12. Effect of turbine inlet temperature (T_6) on integrated system: (a) exergy efficiency; (b) exergy destruction factor.

% to 1.05 %. This is the result of the reduction in T_{out1} and the power generation capacity of SCO_2-BC module. Furthermore, the exergy efficiency of Cu-Cl module ($\eta_{ex,Cu-Cl}$) is reduced from 73.11 % to 71.50 %, and the exergy destruction factor (φ_{Cu-Cl}) is reduced from 7.15 % to 6.35 %. This is because the increase in S_2 leads to decrease both in T_{out1} and T_{out2}. As a result, hydrogen production, power consumption, and the amount of hot water required for hydrogen production all decrease. Consequently, as S_2 increases, $\eta_{ex,Cu-Cl}$ and φ_{Cu-Cl} decrease. It shows appropriately increasing S_2 is beneficial to reducing exergy destruction.

The parameters of S_1=0.01 m^2, S_2=3.0 m^2, C=400 and R_{O2}=0.21 were set to discuss the influence of turbine inlet temperature (T_6) on integrated system. Fig. 12 shows that increasing T_6 from 950 K to 1125 K does not affect TPV module, $\eta_{ex,TPVs}$ is maintained for 57.97 %, and φ_{TPVs} is maintained for 29.20 %. Besides, η_{ex,SCO_2} increases from 76.20 % to 82.76 %, and φ_{SCO_2} is reduced from 2.59 % to 1.34 %. The reason is that the increase in T_6 contributes to a rise in T_{out2} while T_{out1} remains constant, and it further causes the reduction in power generation, thus the exergy efficiency increases and the exergy destruction factor decreases. Furthermore, $\eta_{ex,Cu-Cl}$ increases slightly from 68.89 % to 71.75 %, and φ_{Cu-Cl} increases from 3.97 % to 6.45 %. This is because although the increase in T_{out2} increases the denominator of the exergy efficiency of the Cu-Cl module, the hydrogen production, the power consumption and the amount of hot water required for hydrogen production also increase accordingly. As a result, $\eta_{ex,Cu-Cl}$ and φ_{Cu-Cl} increase with T_6.

In general, within the range of S_2=2.0–4.0 m^2 and T_6=950–1125 K, S_2=4.0 m^2 and T_6=1125 K are the most beneficial conditions for reducing the exergy destruction factor of the overall system. η_{ex,SCO_2} is the highest, followed by $\eta_{ex,Cu-Cl}$ and $\eta_{ex,TPVs}$, and the receiver module has the lowest exergy efficiency. For the entire system, φ_{TPVs} is the largest (about 30 %), followed by φ_{TRs} (11.68 %) and φ_{Cu-Cl} (4–7 %), while φ_{SCO_2} is the smallest (1–3 %). Consequently, the system performance can be improved by focusing on optimizing the TPV and the receiver modules.

4.6. Comparison of systems with different configurations

For the purpose of exploring the rationality and superiority of the proposed system, it was compared with two other different configurations: (1) reference system 1 (Ref Sys 1), a power generation system based on TPV and SCO_2-BC; (2) reference system 2 (Ref Sys 2), a hydrogen-electricity cogeneration system based on SCO_2-BC and Cu-Cl cycle. The typical operating conditions of S_1=0.01 m^2, S_2=4.0 m^2, C=400 and R_{O2}=0.21 were selected to explore the effect of turbine inlet temperature (T_6) on the three systems. Electricity/hydrogen production and system efficiency of the three systems were explored, the results are shown in Fig. 13.

From Fig. 13(a), it is presented that the total output power of the proposed system increases with T_6 and the hydrogen power of Cu-Cl module gradually increases from 1.66 kW to 3.16 kW. On the contrary, the electrical power of TPV module is reduced slightly from 7.81 kW to 7.47 kW, and that of SCO_2-BC module is reduced from 1.39 kW to 1.01 kW. It is worth noting that since the Cu-Cl cycle consumes electricity to produce H_2, the electrical power consumed by the Cu-Cl cycle must be subtracted when calculating the overall output power of the system. Therefore, the electrical power of TPV module which is shown in Fig. 13(a) is the values after subtracting the electrical power consumption of Cu-Cl module. Although the electrical power of TPV module is not affected by T_6, the power consumption of Cu-Cl module increases with H_2 production. As a result, if all the electricity is supplied by the TPV module, the final power output of TPV module will decrease. As shown in Fig. 13(b), when T_6 rises, the total output power of the Ref Sys 1 is reduced. Meanwhile, the electrical power of TPV module is maintained for 8.19 kW, and that of the SCO_2-BC module decreases slightly, which is consistent with the electrical power of each module in the proposed system (without considering the electrical power consumption of Cu-Cl module). As presented in Fig. 13(c), when T_6 increases, the total output power of the Ref Sys 2 increases, and the hydrogen power of Cu-Cl module gradually increases from 3.88 kW to 4.59 kW. Meanwhile, the electrical power from SCO_2-BC module remains almost unchanged (within the range of 5.93–5.99 kW). This is because the electrical power consumption of Cu-Cl module is supplied by SCO_2-BC module. Comparing the three systems, it indicates that the total electrical power of the proposed system and Ref Sys 1 is consistent and higher than that of Ref Sys 2, while the hydrogen power of Ref Sys 2 is the highest, and Ref Sys 1 does not produce H_2. As shown in Fig. 13(d), within T_6 range of 950–1125 K, the secondary energy efficiency $\eta_{sec,sys}$ and equivalent electrical efficiency $\eta_{el,sys}$ of the proposed system are higher than the two reference systems (since Ref Sys 1 does not produce hydrogen, its $\eta_{sec,sys}$ and $\eta_{el,sys}$ curves coincide). As T_6 rises, the $\eta_{sec,sys}$ of Ref Sys 1 decreases from 50.42 % to 48.42 %; the $\eta_{sec,sys}$ of Ref Sys 2 increases from 51.70 % to 55.36 %, and the $\eta_{el,sys}$ increases from 41.50 % to 43.28 %. This is because that Ref Sys 1 lacks the Cu-Cl module, so that does not efficiently utilize the energy in the medium and low temperature sections; Ref Sys 2 lacks the TPV module, so that does not efficiently utilize the energy in the high temperature section. The results strongly suggest the

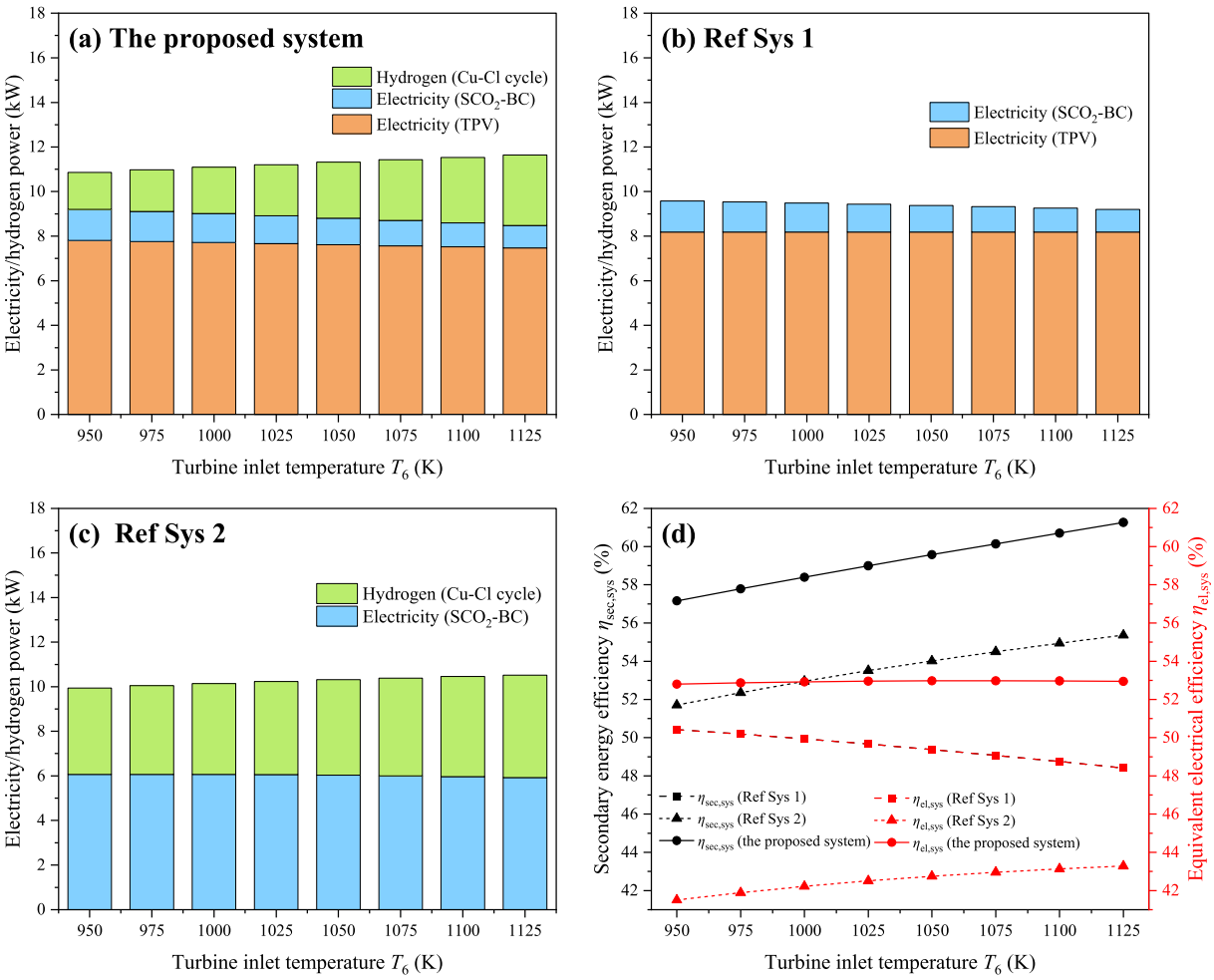

Fig. 13. Electricity/Hydrogen power of different configuration systems: (a) the proposed system, (b) Ref Sys 1, (c) Ref Sys 2; and (d) comparison of system efficiency.

Table 12
Comparison results with previous study of the hydrogen production/hydrogen-electricity cogeneration system.

	Input energy	Products and proportions	Secondary energy efficiency
Zhang [30]	Solar energy	Hydrogen (89.43 %) and electricity (10.57 %)	28.91 %
Abbaspour [59]	Solar energy	Hydrogen (46.16 %), electricity (32.86 %) and superheated steam (20.97 %)	17.48 %
Fang [60]	Solar energy and fuel	Hydrogen (100 %)	55.11 %
Proposed system	Solar energy and fuel	Hydrogen (27.15 %) and electricity (72.85 %)	61.26 %

rationality of the proposed system's configuration, which efficiently and cascade utilizes the photo and thermal energy in each energy quality, realizing efficient hydrogen-electricity cogeneration.

In addition, compared with the hydrogen production/hydrogen-electricity cogeneration systems that have been reported, the proposed system still shows many advantages. The comparison results are shown in Table 12. Zhang et al. [30] proposed a solar thermo-electrochemical water-splitting system for producing hydrogen and electricity. It consists of a solar tower with thermal energy storage (TES) device, a four-step Cu-Cl cycle, a SCO_2-BC and two ORCs. Abbaspour et al. [59] proposed a novel integrated system for hydrogen, electricity and superheated steam production, which combines a solar tower with TES, SCO_2-BC, Cu-Cl cycle and a heat recovery steam generator. Fang et al. [60] proposed a hydrogen production system that combines a trough collector, SOEC, methane steam reforming and Rankine cycle for complementary utilization of methane and full-spectrum solar energy. Compared with these systems, the system proposed in this paper has a higher efficiency and is capable of achieving hydrogen-electricity cogeneration. The system proposed by Zhang and Abbaspour has 100 % solar energy input, their energy loss is relatively large for tower concentrating method. Fang's system can only produce hydrogen, while Abbaspour's system can generate hydrogen, electricity and superheated steam simultaneously. However, the proposed system is not completely green. Furthermore, both the systems of Zhang and Abbaspour adopt TES modules to deal with the instability of solar energy, while the proposed system does not have an energy storage device.

In this study, the system model was established separately by different tools and then coupled, the completeness and unity need to be improved. When facing practical engineering applications, it is necessary to further refine the model and consider environmental factors, and the system design for applications needs to be further optimized. In

future research, the combustion chamber model will be improved, and the chemical mechanism during fuel combustion will be considered for a more detailed temperature distribution. Based on the existing model, it should be continuously optimized the details and further consider heat dissipation, pressure drop, etc. to make it more practical. In addition, the system application design will be optimized, considering the configuration of energy storage devices, and evaluate the energy conservation and emission reduction capabilities of the system, so as to provide better guidance for the development and application of solar high-efficiency hydrogen/electricity cogeneration technology. The combination with renewable energy sources such as biomass and wind energy will also become one of the future development directions of this research.

5. Conclusions

This study proposes solar-gas assisted hydrogen-electricity cogeneration system based on photo-thermal energy cascade conversion. The parametrical thermodynamic analysis on the electricity/hydrogen production efficiency and the system irreversible loss are conducted, and the superiority of the proposed system is discussed. The main conclusions are as follows:

For TPV module, the output power and efficiency of TPV cell both increase with the concentration ratio (C) and receiver area (S_1) for more solar energy input, but it is essential to comprehensively consider safety, economy and efficiency in selecting the appropriate combination of them. Besides, a larger TPV area (S_2) means the greater the TPV output power, while the input energy of the subsequent modules is reduced.

For proposed system, the increase of C, S_2, turbine inlet temperature (T_6) and oxygen ratio (R_{O2}) all have positive effects on the system operation, and C, S_2 and T_6 can be parameters to adjust the ratio of electricity/hydrogen production. Both the secondary energy efficiency and the equivalent electrical efficiency increase with S_2. The secondary energy efficiency ($\eta_{sec,sys}$) increases accordingly with the turbine inlet temperature (T_6), and the equivalent electrical efficiency ($\eta_{el,sys}$) reaches a peak when T_6 is in the range of 975–1025 K. In actual engineering applications, when solar energy input is insufficient (such as cloudy days or nights), the system device can be operated continuously by appropriately increasing R_{O2}. Increasing R_{O2} to about 0.29–0.31, the same $\eta_{sec,sys}$ can be achieved as that with solar input (R_{O2}=0.21); and increasing R_{O2} to about 0.25–0.27, the same $\eta_{el,sys}$ can be achieved as that with solar input (R_{O2}=0.21).

Exergy analysis indicates that the exergy efficiency of SCO_2-BC is the highest, followed by Cu-Cl cycle and TPV module, while the exergy efficiency of receiver module is the lowest. Besides, the exergy destruction factor of TPV module is the largest (about 30 %), followed by receiver module (11.58 %) and Cu-Cl cycle (4–7 %), while that of SCO_2-BC is the smallest (1–3 %). Thus, focusing on optimizing TPV and receiver modules can effectively improve the system performance.

With comprehensive optimized conditions of the proposed system, $\eta_{sec,sys}$ can reach 61.26 %, and $\eta_{el,sys}$ can reach 52.98 %. Compared with different reference systems, the proposed system shows advantages in both $\eta_{sec,sys}$ and $\eta_{el,sys}$. This illustrates the rationality of the proposed system configuration, which can efficiently achieve photo-thermal energy cascade conversion, and is of great significance for the application of efficient and stable hydrogen production from solar energy.

CRediT authorship contribution statement

Zihui Xu: Writing – original draft, Visualization, Validation, Software, Methodology, Investigation, Formal analysis, Data curation. **Shiquan Shan:** Writing – review & editing, Supervision, Resources, Project administration, Methodology, Investigation, Funding acquisition, Conceptualization. **Biao Zhang:** Writing – review & editing, Software, Methodology, Investigation. **Zhihua Wang:** Writing – review & editing, Resources. **Zhijun Zhou:** Writing – review & editing, Resources. **Kefa Cen:** Resources.

Declaration of competing interest

The authors declare that they have no known competing financial interests or personal relationships that could have appeared to influence the work reported in this paper.

Acknowledgments

This work was supported by Natural Science Foundation of Zhejiang Province (LZ25E060001), National Natural Science Foundation of China (52206175), National Key Research and Development Program of China (2023YFB4102800), Fundamental Research Funds for the Central Universities (2022ZFJH04) and Intellectual Property Fund of Zhejiang University.

Appendix

According to thermal balance, the calculation processes of the solar-heat cascade hydrogen-power cogeneration system with complementary solar energy and natural gas is shown in Fig. A1.

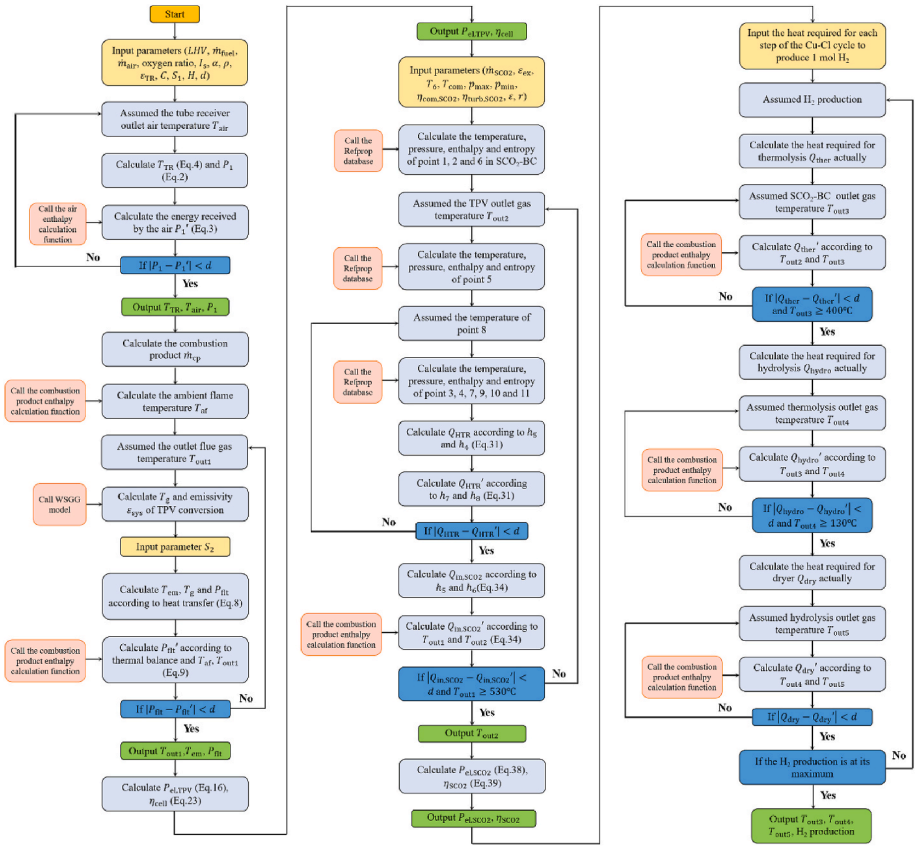

Fig. A1. Flow chart of thermal-balance calculation.

References

[1] M. Shahbaz, K. Dong, D. Balsalobre-Lorente, et al., Recent developments in green finance. Green Growth and Carbon Neutrality, 2023.

[2] S. Su, H. Lu, L. Zhang, et al., Solar energy utilization patterns for different district typologies using multi-objective optimization: a comparative study in China, Sol. Energy 155 (2017) 246–258.

[3] M. Milanese, M. Torresi, G. Colangelo, et al., Numerical analysis of a solar air preheating coal combustion system for power generation, J. Energy Eng. 144 (4) (2018) 04018038.

[4] A. Chinnici, G. Nathan, B. Dally, Experimental demonstration of the hybrid solar receiver combustor, Appl. Energy 224 (2018) 426–437.

[5] Y. Zhao, H. Hong, H. Jin, Mid and low-temperature solar–coal hybridization mechanism and validation, Energy (Calg.) 74 (2014) 78–87.

[6] A. Rovira, C. Sánchez, M. Valdés, et al., Comparison of different technologies for integrated solar combined cycles: analysis of concentrating technology and solar integration, Energies 11 (5) (2018) 1064.

[7] M. Bustamante, W. Liao, A self-sustaining high-strength wastewater treatment system using solar-bio-hybrid power generation, Bioresour. Technol. 234 (2017) 415–423.

[8] X. Xue, W. Han, C. Liu, et al., Proposal and evaluation of a hydrogen and electricity cogeneration system based on thermochemical complementary utilization of coal and solar energy, Energy Convers. Manag. 291 (2023) 117266.

[9] Q. Wang, L. Duan, Z. Lu, et al., Thermodynamic and economic analysis of a multi-energy complementary distributed CCHP system coupled with solar thermochemistry and active energy storage regulation process, Energy Convers. Manag. 292 (2023) 117429.

[10] X. Wang, Q. Liu, Z. Bai, et al., Thermodynamic investigations of the supercritical CO2 system with solar energy and biomass, Appl. Energy 227 (1) (2018) 108–118.

[11] S. Shan, J. Tian, B. Chen, et al., Theoretical and technical analysis of the photo-thermal energy cascade conversion for fuel with high-temperature combustion, Energy (Calg.) 263 (D) (2023) 125990.

[12] S. Shan, Z. Zhou, Z. Wang, et al., New oxy-fuel cascade thermo-photovoltaic energy conversion system: effect of cascade design and oxygen ratio, Energy Convers. Manag. 196 (2019) 1208–1221.

[13] S. Shan, Z. Zhou, K. Cen, An innovative integrated system concept between oxy-fuel thermo-photovoltaic device and a Brayton-Rankine combined cycle and its preliminary thermodynamic analysis, Energy Convers. Manag. 180 (2019) 1139–1152.

[14] H. Ni, X. Qu, G. Zhao, et al., Study of two innovative hydrogen and electricity co-production systems based on very-high-temperature gas-cooled reactors, Energy (Calg.) 273 (15) (2023) 127206.

[15] Q. Wang, R. Macián-Juan, M. Yang, et al., Thermo-economic characteristics and cost-influencing mechanism analysis of an advanced nuclear-powered zero-carbon hydrogen-electricity co-production system with sulfur-iodine process and combined cycle, Int. J. Hydrogen Energy 78 (12) (2024) 688–702.

[16] S. Zhang, G. Liu, Thermal design and performance optimization of the four-step Cu-Cl cycle coupled with clean energy for hydrogen production, J. Clean. Prod. 422 (2023) 138593.

[17] B. Parkinson, P. Balcombe, J. Speirs, et al., Levelized cost of CO2 mitigation from hydrogen production routes, Energy Environ. Sci. 12 (1) (2019) 19–40.

[18] Z. Wang, G. Naterer, K. Gabriel, et al., Comparison of sulfur-iodine and copper-chlorine thermochemical hydrogen production cycles, Int. J. Hydrogen Energy 35 (10) (2010) 4820–4830.

[19] H. Ishaq, I. Dincer, A comparative evaluation of three Cu-Cl cycles for hydrogen production, Int. J. Hydrogen Energy 44 (16) (2019) 7958–7968.

[20] H. Ishaq, I. Dincer, G. Naterer, Development and assessment of a solar, wind and hydrogen hybrid trigeneration system, Int. J. Hydrogen Energy 43 (52) (2018) 23148–23160.

[21] H. Sayyaadi, M. Boroujeni, Conceptual design, process integration, and optimization of a solar CuCl thermochemical hydrogen production plant, Int. J. Hydrogen Energy 42 (5) (2017) 2771–2789.

[22] S. Sadeghi, S. Ghandehariun, Thermodynamic analysis and optimization of an integrated solar thermochemical hydrogen production system, Int. J. Hydrogen Energy 45 (53) (2020) 28426–28436.

[23] S. Coulibaly, Y. Tang, S. Camara, et al., A theoretical study of molten carbonate fuel cell combined with a solar power plant and Cu-Cl thermochemical cycle based on techno-economic analysis, Int. J. Hydrogen Energy 47 (54) (2022) 22680–22690.
[24] S. Sadeghi, S. Ghandehariun, A standalone solar thermochemical water splitting hydrogen plant with high-temperature molten salt: thermodynamic and economic analyses and multi-objective optimization, Energy (Calg.) 240 (1) (2022) 122723.
[25] J. Guo, M. Li, Y. He, et al., A systematic review of supercritical carbon dioxide(S-CO2) power cycle for energy industries: technologies, key issues, and potential prospects, Energy Convers. Manag. 258 (2022) 115437.
[26] M. Li, H. Zhu, J. Guo, et al., The development technology and applications of supercritical CO2 power cycle in nuclear energy, solar energy and other energy industries, Appl. Therm. Eng. 126 (5) (2017) 255–275.
[27] S. Shan, B. Chen, J. Tian, et al., Improving the performance of steam power cycle through thermo-photovoltaic device: a novel combined system and thermodynamic analysis, Energy Convers. Manag. 269 (2022) 116139.
[28] C. Turchi, Z. Ma, J. Dyreby, Supercritical carbon dioxide power cycle configurations for use in concentrating solar power systems. Proceedings of the ASME Turbo Expo 2012: Turbine Technical Conference and Exposition. Volume 5: Manufacturing Materials and Metallurgy; Marine; Microturbines and Small Turbomachinery; Supercritical CO2 Power Cycles. Copenhagen, Denmark, 2012; June 11-15, pp. 967–973.
[29] X. Sun, X. Li, J. Zeng, et al., Energy and exergy analysis of a novel solar-hydrogen production system with S–I thermochemical cycle, Energy (Calg.) 283 (15) (2023) 128737.
[30] S. Zhang, K. Li, P. Zhu, et al., An efficient hydrogen production process using solar thermo-electrochemical water-splitting cycle and its techno-economic analyses and multi-objective optimization, Energy Convers. Manag. 266 (2022) 115859.
[31] F. Sorgulu, I. Dincer, A solar energy driven thermochemical cycle based integrated system for hydrogen production, Energy (Calg.) 269 (2023) 126834.
[32] H. Song, H. Wang, H. Zheng, et al., Analysis of cascade and hybrid processes for hydrogen production by full spectrum solar energy utilization, Energy Convers. Manag. 291 (2023) 117289.
[33] S. Jia, S. Shan, F. Zhang, et al., Parametrical analysis of a novel CHP system based on solar-gas assisted thermo-photovoltaic device, Energy Convers. Manag. 271 (2022) 116316.
[34] F. Wang, Z. Tang, X. Gong, et al., Heat transfer performance enhancement and thermal strain restrain of tube receiver for parabolic trough solar collector by using asymmetric outward convex corrugated tube, Energy (Calg.) 114 (2016) 275–292.
[35] J. Osorio, A. Rivera-Alvarez, J. Ordonez, Effect of the concentration ratio on energetic and exergetic performance of concentrating solar collectors with integrated transparent insulation materials, Sustain. Energy Technol. Assessments 32 (2019) 58–70.
[36] R. Forristall, Heat Transfer Analysis and Modeling of a Parabolic Trough Solar Receiver Implemented in Engineering Equation Solver, National Renewable Energy Lab, Golden, CO, 2003 (US).
[37] R. Stephen, An Introduction to Combustion: Concepts and Applications, McGrw-Hill Companies, Inc, 2000.
[38] H. Daneshvar, R. Prinja, N. Kherani, Thermophotovoltaics: fundamentals, challenges and prospects, Appl. Energy 159 (1) (2015) 560–575.
[39] S. Shan, S. Jia, Z. Fan, et al., A novel solar-fuel assisted thermophotovoltaic system and parametrical analysis, Therm. Sci. 27 (4A) (2023) 2691–2705.
[40] S. Shan, B. Qian, Z. Zhou, et al., New pressurized WSGG model and the effect of pressure on the radiation heat transfer of H_2O/CO_2 gas mixtures, Int. J. Heat Mass Tran. 121 (2018) 999–1010.
[41] Y. Zhang, Q. Li, H. Zhou, Theory and Calculation of Heat Transfer in Furnaces, Elsevier Inc, 2016.
[42] C. Algora, E. Ortiz, I. Rey-Stolle, et al., A GaAs solar cell with an efficiency of 26.2% at 1000 suns and 25.0% at 2000 suns, IEEE Trans. Electron. Dev. 48 (5) (2002) 840–844.
[43] E. Shoaei, Performance assessment of thermophotovoltaic application in steel industry, Sol. Energy Mater. Sol. Cell. 157 (2016) 55–64.
[44] J. Song, X. Li, X. Ren, C. Gu, Performance analysis and parametric optimization of supercritical carbon dioxide ($S\text{-}CO_2$) cycle with bottoming Organic Rankine Cycle (ORC), Energy (Calg.) 143 (2018) 406–416.
[45] J. Xu, E. Sun, M. Li, et al., Key issues and solution strategies for supercritical carbon dioxide coal fired power plant, Energy (Calg.) (2018) 227–246, 1572018.
[46] L. Sun, Y. Wang, D. Wang, et al., Parametrized analysis and multi-objective optimization of supercritical CO_2 (S-CO2) power cycles coupled with parabolic trough collectors, Appl. Sci. 10 (9) (2020) 3123.
[47] B. Zhang, S. Shan, Z. Zhou, A novel clean hydrogen production system combining cascading solar spectral radiation and copper-chlorine cycle: modeling and analysis, J. Clean. Prod. 380 (2022) 135036.
[48] F. Razi, I. Dincer, K. Gabriel, Process improvement and analysis of an integrated four-step copper-chlorine cycle modified with a flash vaporization process for hydrogen production, Energy Fuel. 35 (10) (2021) 9038–9046.
[49] M. Orhan, İ. Dinçer, M. Rosen, Efficiency comparison of various design schemes for copper–chlorine (Cu-Cl) hydrogen production processes using aspen plus software, Energy Convers. Manag. 63 (2012) 70–86.
[50] M. Ferrandon, M. Lewis, D. Tatterson, et al., The hybrid Cu-Cl thermochemical cycle. I. Conceptual process design and H2A cost analysis. II. Limiting the formation of CuCl during hydrolysis, in: Proceedings of the American Institute of Chemical Engineers Annual Meeting, November 2008, pp. 16–21. Philadelphia, PA, USA.
[51] H. Ishaq, I. Dincer, G. Naterer, Multigeneration system exergy analysis and thermal management of an industrial glassmaking process linked with a Cu-Cl cycle for hydrogen production, Int. J. Hydrogen Energy 44 (2019) 9791–9801.
[52] D. Pashchenko, Green hydrogen as a power plant fuel: what is energy efficiency from production to utilization? Renew. Energy 223 (2024) 120033.
[53] S. Mousavi, M. Mehrpooya, M. Rad, et al., A new decision-making process by integration of exergy analysis and techno-economic optimization tool for the evaluation of hybrid renewable systems, Sustain. Energy Technol. Assessments 45 (2021) 101196.
[54] R.U. Ayres, L.W. Ayres, K. Martinas, Eco-Thermodynamics: Exergy and Life Cycle Analysis, 1996.
[55] T. Gholizadeh, M. Vajdi, F. Mohammadkhani, Thermodynamic and thermoeconomic analysis of basic and modified power generation systems fueled by biogas, Energy Convers. Manag. 181 (2019) 463–475.
[56] M. Salim, M. Saeed, M. Kim, Performance analysis of the supercritical carbon dioxide Re-compression Brayton cycle, Appl. Sci. 10 (3) (2020) 1129.
[57] M. Quero, R. Korzynietz, M. Ebert, et al., Solugas-operation experience of the first solar hybrid gas turbine system at MW scale, Energy Proc. 49 (2014) 1820–1830.
[58] T. Liu, J. Yang, Z. Yang, et al., Multiparameter optimization and configuration comparison of supercritical CO2 Brayton cycles based on efficiency and cost tradeoff, Sci. China Technol. Sci. 64 (2021) 2084–2098.
[59] G. Abbaspour, H. Ghaebi, B. Ziapour, Energy and exergy analysis of a new solar hybrid system for hydrogen, power and superheated steam production, Renew. Energy 237 (B) (2024) 121723.
[60] J. Fang, M. Yang, L. Cui, et al., Efficient hydrogen production system with complementary utilization of methane and full-spectrum solar energy, Energy Convers. Manag. 283 (2023) 116951.